



**HAL**  
open science

## Role of interlayer porosity and particle organization in the diffusion of water in swelling clays

A. Asaad, F. Hubert, E. Ferrage, T. Dabat, E. Paineau, P. Porion, S. Savoye, B. Gregoire, B. Dazas, Alfred Delville, et al.

### ► To cite this version:

A. Asaad, F. Hubert, E. Ferrage, T. Dabat, E. Paineau, et al.. Role of interlayer porosity and particle organization in the diffusion of water in swelling clays. *Applied Clay Science*, 2021, 207, pp.106089. 10.1016/j.clay.2021.106089 . hal-03212181

**HAL Id: hal-03212181**

**<https://hal.science/hal-03212181>**

Submitted on 29 Apr 2021

**HAL** is a multi-disciplinary open access archive for the deposit and dissemination of scientific research documents, whether they are published or not. The documents may come from teaching and research institutions in France or abroad, or from public or private research centers.

L'archive ouverte pluridisciplinaire **HAL**, est destinée au dépôt et à la diffusion de documents scientifiques de niveau recherche, publiés ou non, émanant des établissements d'enseignement et de recherche français ou étrangers, des laboratoires publics ou privés.

1 **Role of interlayer porosity and particle organization in the diffusion of**  
2 **water in swelling clays**

3  
4 A. Asaad<sup>1,\*</sup>, F. Hubert<sup>1</sup>, E. Ferrage<sup>1</sup>, T. Dabat<sup>1</sup>, E. Paineau<sup>2</sup>, P. Porion<sup>3</sup>, S. Savoye<sup>4</sup>, B.  
5 Gregoire<sup>1</sup>, B. Dazas<sup>1</sup>, A. Delville<sup>3</sup>, E. Tertre<sup>1,\*</sup>

6  
7 <sup>1</sup> IC2MP, Equipe HydrASA, UMR 7285 CNRS/Université de Poitiers, 86073 Poitiers, France.

8 <sup>2</sup> Université Paris-Saclay, CNRS, Laboratoire de Physique des Solides, 91405 Orsay, France

9 <sup>3</sup> ICMN, UMR 7374 CNRS/Université d'Orléans, 45071 Orléans, France

10 <sup>4</sup> Université Paris-Saclay, CEA, Service d'Etude du Comportement de Radionucléides, 91191  
11 Gif-sur-Yvette, France

12  
13 \* E-mail addresses of the corresponding authors:

14 A. Asaad: ali.asaad@univ-poitiers.fr

15 E. Tertre: emmanuel.tertre@univ-poitiers.fr

16  
17  
18 **Highlights**

19 - Samples with same interparticle porosity but different particle organizations.

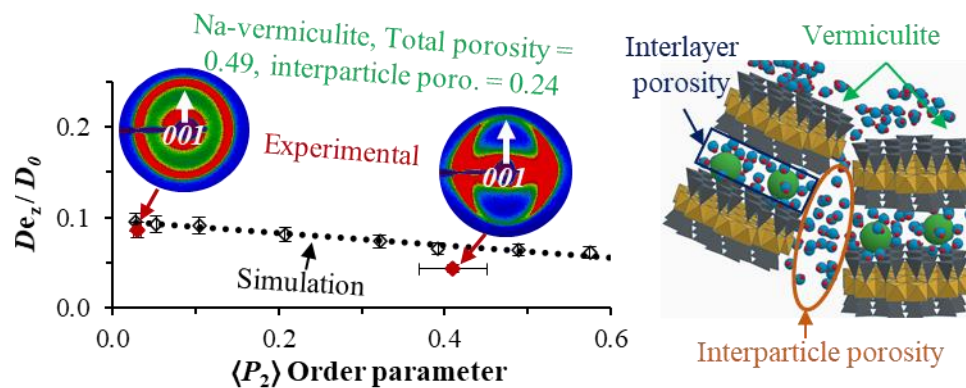
20 - Reduction in the overall mobility of water in presence of interlayer porosity.

21 - Minor role of interlayer porosity in flux traversing samples.

22 - Anisotropy in water diffusion quantitatively related to the preferential orientation of the  
23 particles.

24

## 25 Graphical abstract



## 26 Abstract

27 This study focuses on the role played by the interparticle and interlayer porosities, and the  
28 preferred orientation of the particles on water diffusion in dual-porosity clayey media (i.e.,  
29 swelling clay minerals). For this purpose, we use Na-vermiculite, a swelling clay that does not  
30 exhibit osmotic swelling and therefore allows a clear discrimination between the interparticle  
31 and interlayer porosities. Two samples were prepared with an equal proportion of interparticle  
32 and interlayer porosities (i.e., 0.25 each) but different degree of preferred particle orientation  
33 (i.e., isotropic vs anisotropic). Through-diffusion and pulsed gradient spin echo attenuation  
34 measurements by nuclear magnetic resonance of protons techniques were used to probe water  
35 mobility, while the orientation of the particles was quantified by X-ray scattering analysis.  
36 Experimental water diffusion results obtained with these two Na-vermiculite samples were  
37 compared to those with samples made of Na-kaolinite particles (non-swelling clay mineral)  
38 having only interparticle porosities equal to 0.25 and 0.5, corresponding respectively to the  
39 interparticle and the total porosity of the Na-vermiculite samples. In addition, these  
40 experimental results were compared to simulated data using Brownian dynamics with virtual  
41 porous media representative of the real samples. For the range of porosities investigated, a good  
42 agreement was observed between measured and simulated water mobilities. The obtained  
43 results confirmed the important role played by the preferential orientation of the particles on  
44 water dynamics in clayey media, through an important reduction of overall water mobility

45 between the isotropic and anisotropic Na-vermiculite samples. These results also showed that  
46 for the same total porosity, the presence of interlayer porosity and associated nano-confinement  
47 led to a logical reduction in the pore diffusion coefficient of water in Na-vermiculite in  
48 comparison to Na-kaolinite. Moreover, in comparison with Na-kaolinite having the same  
49 interparticle porosity, results showed that the contribution of the interlayer volume on the  
50 traversing flux was small compared to the interparticle volume. Finally, the computed results  
51 revealed that the anisotropy in water diffusion can be directly predicted based on the degree of  
52 particles preferred orientation, irrespective of the total or the distribution of the different  
53 porosity types.

## 54 **1. Introduction**

55 Diffusion is the main transport process in compacted clayey rocks owing to their low  
56 hydraulic conductivity (Pusch, 1979; Bourg et al., 2003; Bourg and Tournassat, 2015). This  
57 process has been extensively studied, especially in the context of the storage of nuclear waste  
58 and CO<sub>2</sub>, and resulted in an abundance of experimental data obtained by various methods (such  
59 as through-diffusion (TD) experiments using tracers or quasi-elastic neutron scattering) and  
60 models describing the diffusion of different elements in clayey media (e.g., Sato and Suzuki,  
61 2003; Van Loon et al., 2004; Andra, 2005; García-Gutiérrez et al., 2006; Landais, 2006; Bachu,  
62 2008; González Sánchez et al., 2008a and b; Glaus et al., 2010; Gimmi and Kosakowski, 2011;  
63 Altmann et al., 2015; Savoye et al., 2015; Charlet et al., 2017; Bestel et al., 2018; Dagnelie et  
64 al., 2018). Note that these data were obtained for various media constitutive of mono- or multi-  
65 clayey phases and considering the presence or not of non-clayey minerals (Shackelford and  
66 Moore, 2013; Bourg and Tournassat, 2015; Charlet et al., 2017; Bestel et al., 2018 and  
67 references therein).

68 The organization and connectivity of the pore network are the main parameters that  
69 control diffusion of water in clayey media since water is usually inert from a chemical

70 viewpoint ([Bourg and Tournassat, 2015](#) and references therein). The influence of the total  
71 porosity value is the parameter that has been the subject of most extensive investigation. Thus,  
72 a logical decrease in the water diffusion coefficients with a diminution in the porosity is  
73 commonly reported (e.g., [Tournassat and Steefel, 2019](#) and references therein). In contrast, less  
74 attention has been paid to the influence of other parameters, such as the preferential orientation  
75 of the clay particles, a typical property of these platelet materials in natural aqueous  
76 environments ([Bennett et al., 1981](#)), or to the distribution of different types of porosities (e.g.,  
77 interlayer vs. interparticle porosity in swelling clay minerals). Nevertheless, by investigating  
78 the spatial anisotropy of the diffusion of water tracers in such media, either by TD experiments  
79 or by analyzing the 3D distribution of the tracer, several authors ([Farver and Yund, 1999](#); [Sato,](#)  
80 [2000](#); [Sato and Suzuki, 2003](#); [Suzuki et al., 2004](#); [García-Gutiérrez et al., 2006](#); [Wenk et al.,](#)  
81 [2008](#); [Wittebroodt et al., 2012](#); [Xiang et al., 2013](#); [Jacops et al., 2017](#); [Dagnelie et al., 2017](#))  
82 have reported a significant diminution of the effective diffusion coefficients ( $De$ ) of water in  
83 the direction perpendicular to the sedimentation beds with respect to the parallel direction. Such  
84 behavior was attributed to anisotropy in the shape and distribution of the pores between clay  
85 particles, resulting from their preferred orientation, as evidenced by either X-ray scattering  
86 (XRS, [Wenk et al., 2008](#)) or microscopy-imaging techniques ([Sato, 2000](#); [Suzuki et al., 2004](#)).

87         The porosity and preferred orientation of the particles in clayey media are often coupled  
88 parameters (a decrease in the porosity leads to an increase in the particle orientation). Hence, it  
89 is complicated to discriminate the contribution of each parameter to the overall diffusion  
90 process. To overcome such limitation, [Dabat et al., \(2020\)](#) recently proposed a methodology  
91 that allow to prepare samples from Na-kaolinite particles (non-porous and non-charged  
92 particles) with similar porosity but different degrees of preferential orientation of the particles.  
93 These authors succeeded in connecting the anisotropy of the tensor diffusion of the water tracer  
94 to the preferential orientation of the particles in these samples for a porosity value of  $\sim 0.5$  based

95 on experimental water diffusion analyses obtained using pulsed gradient spin echo attenuation  
96 measurements by nuclear magnetic resonance (PGSE-NMR) and numerical data from  
97 Brownian dynamics (BD) simulations using various virtual porous media (VPMs). However,  
98 such a relationship remains to be investigated in the case of clay media made of swelling clay  
99 particles with two types of porosities (i.e., interlayer and interparticle) being accessible for the  
100 water. In such dual-porosity media with charged surfaces, water mobility in the interlayer space  
101 can be drastically reduced compared to that in the interparticle porosity, as revealed by  
102 molecular dynamic simulations (Titiloye and Skipper, 2001; Marry et al., 2002; Malikova et  
103 al., 2006; Michot et al., 2012 among others) and quasi-elastic neutron scattering studies  
104 (González Sánchez et al., 2008a; Bestel, 2014) performed on low charge swelling clays, e.g.  
105 montmorillonite. Note that this reduced mobility near the surface of the charged clayey particles  
106 is usually considered in reactive transport models (i.e., models that couple transport to chemical  
107 properties using continuum approaches (Ochs et al., 2001; Tournassat and Steefel, 2019 and  
108 references therein), which predict the diffusion of water in complex and heterogenous clayey  
109 media. The use of these numerical approaches allow for decoupling the diffusion that occurs in  
110 the different types of porosity (i.e., interlayer vs. interparticle porosities), while discrete models  
111 (e.g., molecular dynamics, random walk or BD simulations) also allow consideration of the  
112 specific role of the particles' preferred orientation on the diffusion properties (e.g., Churakov  
113 and Gimmi, 2011; Tyagi et al., 2013; Bacle et al., 2016; Gimmi and Churakov, 2019; Dabat et  
114 al., 2020; Underwood and Bourg, 2020). Beyond such numerical approaches, existing  
115 experimental water diffusion data in dual-porosity media were almost exclusively obtained with  
116 smectite particles (e.g., Bourg and Tournassat, 2015 and references therein). This mineral  
117 displays, however, osmotic swelling in water-saturated conditions (i.e., incorporation of an ill-  
118 defined number of water molecules between the layers (Abend and Lagaly, 2000; Liu, 2013;  
119 Tertre et al., 2018 among others), which hampers the calculation of the respective interlayer

120 and interparticle porosity volumes. In the scope of quantitatively discussing the role played by  
121 interlayer and interparticle porosities on the diffusion of water, as well as by the preferred  
122 orientation of the clay particles, additional experimental data on dual-porosity clay media that  
123 are not sensitive to osmotic swelling are required. For this purpose, vermiculite clay mineral  
124 represents an ideal candidate. Vermiculite is a swelling clay mineral with a structure similar to  
125 smectite. However, owing to the higher layer charge, this mineral does not display osmotic  
126 swelling (Faurel, 2012) and exhibits well-defined interlayer volumes in water-saturated  
127 conditions, which allows for a better determination of the different interlayer and interparticle  
128 volumes in the samples. Tertre et al. (2018) used this mineral to perform water tracer diffusion  
129 experiments and highlighted the notable differences in the effective diffusion coefficients  
130 obtained in vermiculite compared to montmorillonite for similar total porosities. Moreover, by  
131 comparison with experimental data reported for kaolinite, these authors noticed that the  
132 experimental data were similar for the same interparticle porosity value. However, because the  
133 preferred orientation of the clay particles was not measured, it was not possible to deduce  
134 information on the contribution of different parameters (the porosity distribution or particles'  
135 orientation) to the overall water diffusion process.

136 The present study represents an extension of the work of Tertre et al. (2018) and the recent  
137 approach proposed by Dabat et al. (2020) for kaolinite clay mineral (at a porosity value of  $\sim 0.5$ ),  
138 to the dual-porosity media made of Na-vermiculite particles. In this work, an experimental  
139 methodology was developed to obtain vermiculite samples with two degrees of preferential  
140 particle orientation, as measured by XRS analysis, for the same total porosity of 50% (the same  
141 total porosity used by Dabat et al. (2020) for Na-kaolinite samples). In such conditions, Na-  
142 vermiculite is composed of an equal proportion of interlayer and interparticle porosity  
143 proportions (i.e.,  $\sim 0.25$ ). Experimental diffusion data on water tracer (HDO) in these media  
144 were obtained using TD experiments that allow to determine the effective diffusion coefficients

145 in the direction perpendicular to the sedimentation plane of the particles. To complete the  
146 experimental dataset on water diffusion, the sample set also included an additional clay medium  
147 of Na-kaolinite with a total porosity of  $\sim 0.25$  (i.e., similar interparticle porosity as with Na-  
148 vermiculite). For this sample, both the TD and PGSE-NMR results on water diffusion were  
149 obtained to assess the concordance of the two methods on the analysis of water diffusion despite  
150 the significant difference in the timescales probed for water dynamics (i.e., ms and days for the  
151 PGSE-NMR and TD experiments, respectively). Following a coupled experimental-  
152 computational approach (Dabat et al., 2020), all these data were systematically compared to the  
153 results obtained by BD simulations, which were performed with 3D virtual porous media,  
154 generated to mimic the real ones in term of mineralogy and porosity distribution, while also  
155 covering a large range of anisotropy degrees in particle orientations.

## 156 **2. Materials and Methods**

### 157 **2.1. Materials**

158 The vermiculite used in this study is from Santa Olalla (Huelva, Spain; González García  
159 and García Ramos, 1960; De La Calle et al., 1977). In its original form, the centimetric  
160 vermiculite crystals are  $Mg^{2+}$ -saturated with a structural formula (Marcos et al., 2003; Arguelles  
161 et al., 2010):  $[(Mg_{4.92}Fe_{0.44}Al_{0.60}Ti_{0.04})(Si_{5.66}Al_{2.34})O_{20}(OH)_4](Mg_{0.76}Ca_{0.06}Na_{0.04}), 7.63H_2O]$ .  
162 The 0.1-0.2  $\mu m$  particle size fraction, used for this study, was obtained by sonication and  
163 centrifugation methods using the protocol established by Reinholdt et al., (2013). The kaolinite  
164 used is KGa-2 from the Source Clay Repository of the Clay Mineral Society, with an average  
165 size of the particles of approximately 0.5  $\mu m$  (Hassan et al., 2005), and a structural formula  
166 (Mermut and Cano, 2001) of  $[(Al_{3.80}Ti_{0.13}Fe^{3+}_{0.07})(Si_{3.84}Al_{0.16})O_5(OH)_4]$ .

167 Both materials were exchanged into homoionic  $Na^+$  form (i.e., Na-kaolinite and Na-  
168 vermiculite) using five saturation cycles with a 1-M NaCl solution, followed by removal of  
169 excess of salt by dialysis using a 6-8 KD membrane until test with silver nitrate was negative.

170 Compacted samples were prepared from the dialyzed clay dispersion dried at 60°C and then  
171 sieved through a 50 µm mesh to remove the coarsest aggregates. A centrifuged sample made of  
172 Na-vermiculite particles was prepared directly from the dialyzed dispersion and was then stored  
173 at 4°C.

## 174 **2.2. Preparation of samples with contrasted anisotropy in particle orientation**

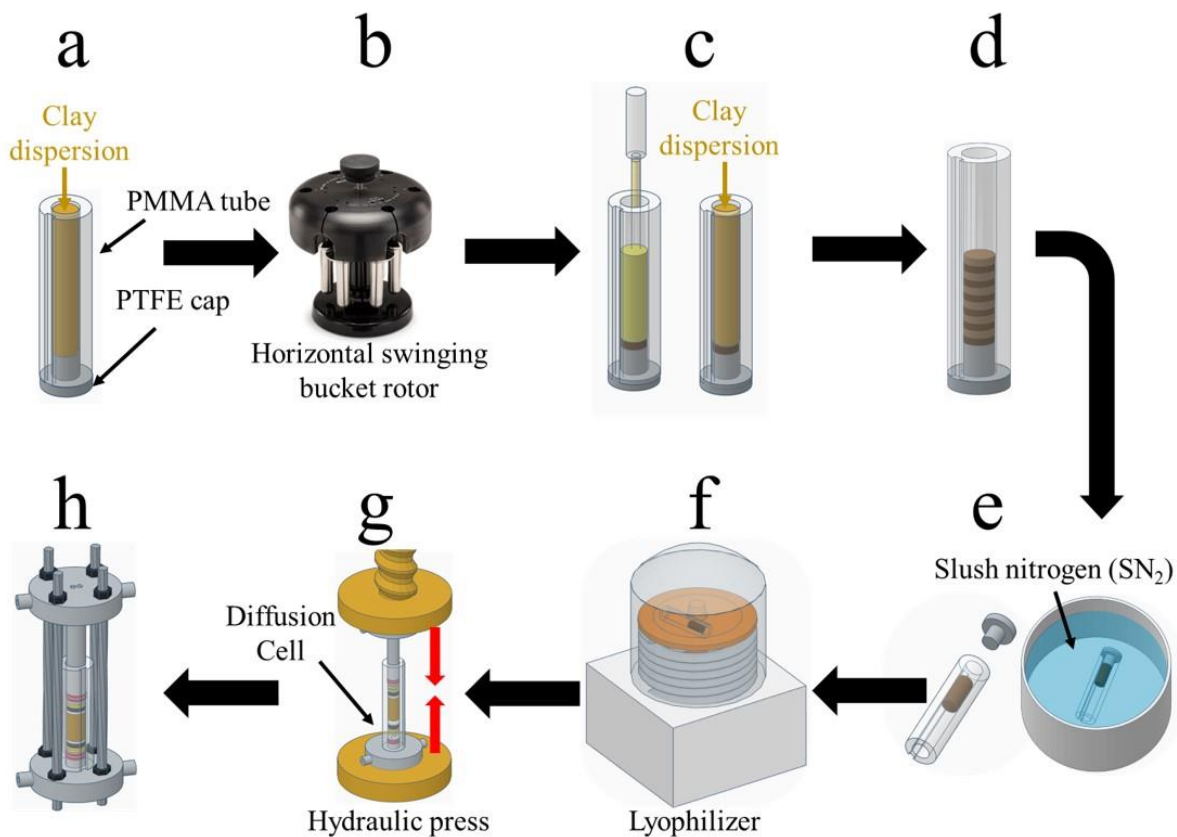
175 The methodology used to prepare compacted Na-kaolinite for PGSE-NMR experiments  
176 as well as experimental setup and acquisition conditions are detailed in section S1.1 in  
177 Supplementary Data (S. D.). For TD experiments, the isotropic samples were prepared by  
178 uniaxial compaction of dried clay powder in (poly)methyl methacrylate (PMMA) tubes  
179 (diameter of 0.95 cm and a height of 7 cm) as in Tertre et al. (2018). By contrast, a new protocol  
180 was developed in the present study to build an anisotropic Na-vermiculite medium with the  
181 same total porosity ( $\epsilon$ ) as the one obtained by compaction. This protocol is illustrated in Fig. 1  
182 and was developed based on the centrifugation process used by Dabat et al., (2020) to prepare  
183 Na-kaolinite samples. It first consists of transferring 3 mL of Na-vermiculite dispersion  
184 (20 g/L) into PMMA tube designed to be mounted directly into the TD cell to avoid sample  
185 transfer and the associated potential damage (Fig. 1a). After a horizontal centrifugation run at  
186 ~23850 g for 25 minutes (Centrifuge Avanti J 301, rotor JS-24.38 from Beckman Coulter® (Fig.  
187 1b)), the clear supernatant was removed, and a new aliquot was added (Fig. 1c). These steps  
188 were repeated ten times to obtain a sufficient mass in the tube (Fig. 1d). After centrifugation, it  
189 was necessary to dry the sample to determine its dried mass used in  $\epsilon$  calculation (details in the  
190 next paragraph). However, because drying by heating can introduce an important shrinkage of  
191 samples and distortion of their structure (Loeber, 1992; Durrieu et al., 1997), a methodology  
192 previously developed for clay cakes (Loeber, 1992; Pret, 2003) was applied to preserve, as best  
193 as possible, the geometry and particle organization in the sample. Accordingly, the sample was  
194 first flash frozen by immersion in slush nitrogen (SN<sub>2</sub>) for 2-5 minutes (Fig. 1e) and then dried

195 by lyophilization at  $-40^{\circ}\text{C}$  for 2-3 hours. Complete water removal was insured when the sample  
196 maintained a stable mass during the last hour of lyophilization (Fig. 1f). Finally, the sample  
197 was mounted to the TD cell, uniaxially compressed to the desired height (Fig. 1g-h).

198 The final thickness ( $L$ ) of all samples prepared for this study are reported in Table 1. Total  
199 porosity  $\varepsilon$  was calculated as difference between the sample volume (considering the diameter  
200 of the tube and the sample's  $L$ ), and the volume occupied by the solid only (i.e., clay particles),  
201 which was determined based on the sample dry mass (at the end of the lyophilization process)  
202 and clay grain density. The latter was calculated to be  $2.62\text{ g cm}^{-3}$  for Na-kaolinite based on the  
203 structural formula and the crystal structure parameters refined for KGa-2 kaolinite by Sakharov  
204 et al. (2016) and  $2.73\text{ g cm}^{-3}$  for Na-vermiculite using the ( $a, b$ ) cell parameters and the chemical  
205 composition of the 2:1 layer reported by Arguelles et al. (2010) and the  $c^*$  parameter (i.e., the  
206 basal spacing) value for dehydrated layers at  $10\text{ \AA}$  (Giesecking, 1975). However, Na-vermiculite  
207 displays a mono-hydrated state (1W) at room humidity and a bi-hydrated state (2W) in water-  
208 saturated conditions, respectively (Faurel, 2012). Consequently, two hydrated densities of 2.49  
209 and  $2.24\text{ g cm}^{-3}$  for 1W and 2W Na-vermiculite, respectively were calculated based on water  
210 content and  $c^*$  parameters derived by Faurel. (2012) for 1W ( $4.13\text{ H}_2\text{O}/\text{O}_{20}(\text{OH})_4$ ,  
211  $c^* = 11.97\text{ \AA}$ ) and 2W layers ( $9.9\text{ H}_2\text{O}/\text{O}_{20}(\text{OH})_4$ ,  $c^* = 14.86\text{ \AA}$ ). Note that for Na-kaolinite,  
212 only the interparticle porosity ( $\varepsilon_{\text{interp.}}$ ) is accessible by the water tracer, resulting in  $\varepsilon = \varepsilon_{\text{interp.}}$ ,  
213 whereas Na-vermiculite exhibits both  $\varepsilon_{\text{interp.}}$  and interlayer porosity ( $\varepsilon_{\text{interl.}}$ ). By considering the  
214 difference in the  $c^*$  parameter value between dehydrated layers at  $10\text{ \AA}$  (Giesecking, 1975) and  
215 fully water saturated layers at  $14.86\text{ \AA}$  (Faurel, 2012), the interlayer volume corresponds  
216 approximately to 1/3 of the particle thickness in water-saturated conditions. Consequently, the  
217 proportion of the  $\varepsilon_{\text{interp.}}$  vs.  $\varepsilon_{\text{interl.}}$  porosities for Na-vermiculite (Table 1) can be calculated for  
218 such conditions by using the following relation:

$$219 \quad \varepsilon = \varepsilon_{\text{interp.}} + \varepsilon_{\text{interl.}} = \varepsilon_{\text{interp.}} + (1 - \varepsilon_{\text{interp.}})/3 \quad (1)$$

220 Finally, for each sample used in this study, a duplicate was prepared to be used for  
221 particle organization measurements.



222 **Fig. 1.** Illustration of the methodology used to prepare Na-vermiculite samples with a high degree  
223 of particles' preferred orientation. (a-d) Oriented sample is prepared by 10 runs of centrifugation of Na-  
224 vermiculite dispersion in (poly)methyl methacrylate (PMMA) tubes sealed from the bottom with  
225 (poly)tetrafluoroethylene (PTFE) caps and by removal of the supernatant after each centrifugation run.  
226 (e-f) Preparation of slush nitrogen and freezing of the sample followed by lyophilization. (g-h) Mounting  
227 the sample into the diffusion cell and compaction to a certain thickness to reach the desired total porosity  
228 value (see Section 2.2), the final thickness of the diffusion cell is maintained by threaded rods and nuts.

229

### 230 *2.3. Measurements of preferred orientation of clay particles through the $\langle P_2 \rangle$ order* 231 *parameter*

232 The degree of anisotropy in the orientation of clay particles in the samples used in this  
233 work was obtained from two-dimensional X-Ray Scattering (2D-XRS) patterns recorded from  
234 the duplicate samples. The measurements were performed at the Laboratoire de Physique des  
235 Solides (LPS) - Orsay, France. Sample preparation method (i.e., induration and slicing) and

236 2D-XRS acquisition parameters are detailed in S. D. (S.1.2). In this work, the degree of  
 237 anisotropy in the orientation of clay platelets is reported in terms of  $\langle P_2 \rangle$  order parameter values  
 238 also referred to as the nematic order  $S$  (Dabat et al., 2018; Underwood and Bourg, 2020) or the  
 239 Hermans parameter  $H$  (Hermans and Platzek, 1939). The  $\langle P_2 \rangle$  order parameter can be derived  
 240 from the orientation distribution functions (ODF) (Dabat et al., 2019, 2020 and references  
 241 therein) obtained from 2D-XRS patterns. Briefly, in a spherical coordinate, the orientation of a  
 242 platelet shape clay particle can be defined as a function of two angles:  $\theta$ , which is the azimuthal  
 243 angle between the normal of the particle (vector that is perpendicular to the basal surface of the  
 244 particle) and the  $z$  axis, and  $\Phi$ , the polar angle in the  $(xy)$  plane (Fig. 2a). For particles with  
 245 uniaxial symmetry (i.e., clay particles for which their  $z$  axis is the only symmetry axis as in this  
 246 study, Wenk et al. (2010) and references therein) the probability for a particle orientation over  
 247 all possible  $\Phi$  angle values is equal. Therefore, the orientation of a clay platelet (ODF) can be  
 248 described as a function of only its  $\theta$  angle, i.e.,  $f(\theta)$ , with the following constraints:

$$249 \quad f(\theta) \geq 0 \quad (2)$$

$$250 \quad f(\theta) = f(\pi - \theta) \quad (3)$$

$$251 \quad \int_0^\pi f(\theta) \sin(\theta) d\theta = 1 \quad (4)$$

252 Eqs. (2) and (3) indicate that the ODF is always positive, with the same probability of the  
 253 particles pointing upward or downward. The term  $f(\theta)\sin(\theta)$  in Eq. (4) corresponds to the  
 254 normalization over all the particles in the sample. From the 2D-XRS patterns, the scattered  
 255 intensities ( $I$ ) of the 001 Bragg peak modulated as a function of the angle  $\tau$  (the angle between  
 256 the normal of the incident beam and the surface of the 2D-detector), and the angle  $\theta$  (Fig. 2b).  
 257 Because of the position of the 001 reflection at low scattering angles ( $2\theta_B$ ), the hypothesis  $\theta =$   
 258  $\tau$  is a valid approximation (Dabat et al., 2019). Hence, the ODF  $f(\theta)$  can be expressed from the  
 259 scattered intensity  $I(\theta)$  evolution integrated from the 2D-XRS patterns as follows:

260

$$f(\theta) = \frac{I(\theta)}{\int_0^\pi I(\theta) \sin(\theta) d\theta} \quad (5)$$

261 The ODF  $f(\theta)$  can also be written with a second order Legendre polynomial as follows:

$$\langle P_2 \rangle = \int_0^\pi \langle P_2 \rangle (\cos\theta) \cdot f(\theta) \sin(\theta) d\theta \quad (6)$$

263 Finally, average value of  $\langle P_2 \rangle$  calculated over the angular distribution using Eq. (6), is  
 264 comprised between 0 for an isotropic particle organization and 1 for a perfectly anisotropic  
 265 organization with all particles having the same preferred orientation (i.e., bedding plane).

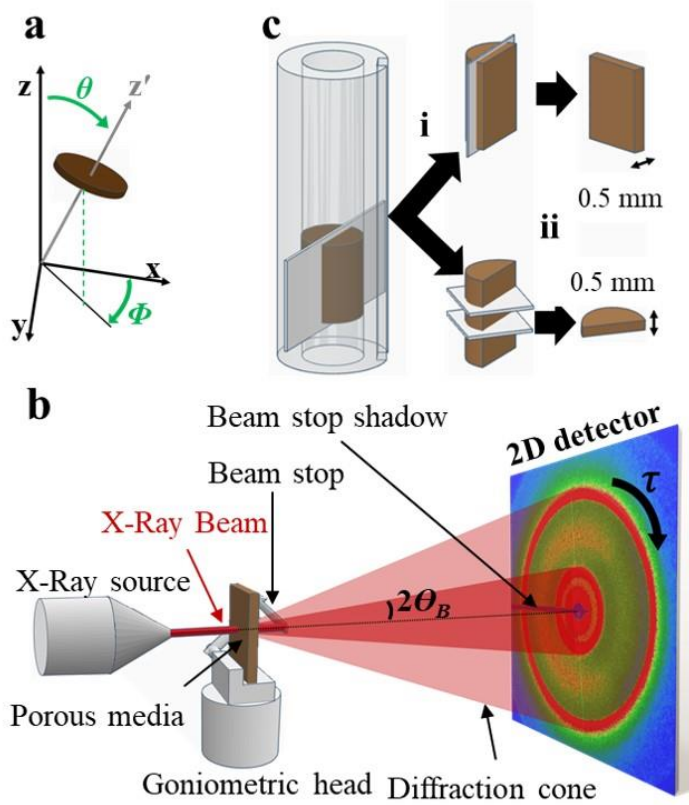


**Fig.2.** Experimental measurement of the particle orientation in clayey samples using an X-ray scattering technique with a 2D-detector (2D-XRS). (a) Spherical coordinates ( $\rho, \theta, \Phi$ ) with respect to the sample tube (laboratory frame:  $(x,y,z)$ ) and the angles ( $\theta, \Phi$ ) describing the orientation of the normal ( $Oz'$ ) of an individual clay particle. (b) The 2D-XRS instrumental setup and measurement of the particle orientation by azimuthal integration (along  $\tau$ ) of the scattered intensity. (c) Illustration of the method to cut the indurated sample into lamellas: (i) the indurated sample is cut into two vertical halves, (ii) cutting the longitudinal and transversal lamellas (the cutting planes are shown in light colour cuboid). The lamellas are reduced to a thickness of 500  $\mu\text{m}$  by polishing.

288 **2.4. Water diffusion measurement in Na-vermiculite and kaolinite samples**

289 Experimental water diffusion coefficients were obtained from Na-vermiculite and Na-  
 290 kaolinite samples using PGSE-NMR and TD of the water tracer (HDO) experiments. Sample  
 291 preparation, acquisition parameters, and data treatment are detailed in the S. D. (sections S.1.1  
 292 and S.1.3, respectively). It is important to note that the analysis of the TD results allow to obtain

293 the effective diffusion coefficient  $De$  of HDO in the  $z$ -direction of the tube ( $De_z$ ), i.e.,  
 294 perpendicular to the compression direction/centrifugation plane of the sample, while the PGSE-  
 295 NMR analysis allows to obtain the pore diffusion coefficients  $Dp_z$  and  $Dp_{x,y}$ .  
 296  $De_z$  is defined from the self- diffusion coefficient of species in bulk water ( $D_0$ ) by the following  
 297 equation (Bear, 1972; Dykhuizen and Casey, 1989; Bourg et al., 2006):

$$298 \quad De = \frac{\varepsilon}{G} D_0 \quad (7)$$

299 where  $\varepsilon$  is the accessible porosity for the tracer, and  $G$  the geometrical factor (tortuosity factor),  
 300 which describes the impact of the pore-network geometry (pore shape, particle orientation,  
 301 connectivity, and constrictively). The pore diffusion  $Dp$  can also be related to  $D_0$  as follows:

$$302 \quad Dp = \frac{1}{G} D_0 \quad (8)$$

303 Hence, in the case of water tracers for which the total porosity is accessible to diffusion and no  
 304 adsorption occurs, the pore and effective diffusion coefficients are related to  $\varepsilon$  as follows:

$$305 \quad De = \varepsilon Dp \quad (9)$$

### 306 **2.5 Brownian dynamics simulations of water diffusion in virtual porous media**

307 Mesoscale Brownian dynamics simulations of water diffusion in both Na-vermiculite and  
 308 Na-kaolinite as a function of the anisotropy in the particles' orientation were performed on 3D  
 309 virtual porous media (VPM). To cover a large range of anisotropy degrees in particle  
 310 orientations, 13 particle packings were generated with  $\langle P_2 \rangle$  values varied from 0.03 to 0.96  
 311 (Ferrage et al., 2018; Dabat et al., 2020); see Table. S1 in S. D., and Fig. 3a), mimicking the  
 312 distribution of the shapes and sizes of the particles in these samples. The description of the  
 313 generation of these VPM is detailed in S.1.4 of S. D.

314 Brownian dynamics simulations were performed according to the methodology detailed  
 315 by Dabat et al. (2020). For the case where the time step  $\delta t$  is much larger than the velocity

316 correlation time  $\gamma_i$  of probe  $i$  (i.e.,  $\gamma_i \delta t \gg 1$ ), and considering the probe's displacements as  
 317 completely independent, the displacement of molecular probes in the framework of the general  
 318 Langevin equation can be reduced as follows (Gunsteren et al., 1981):

$$319 \quad \vec{x}_i(t + \delta t) = \vec{x}_i(t) + \vec{R}_i \quad (10)$$

320 with the random force  $\vec{R}_i$  that satisfies a Gaussian distribution function with zero mean and  
 321 standard deviation given by

$$322 \quad \langle R_i^2 \rangle = 2D_i \delta t \quad (11)$$

323 where  $D_i$  is the molecular self-diffusion of probe  $i$ . For diffusion within unrestricted isotropic  
 324 media, the modulus of the random 3D displacements is quantified by the self-diffusion  
 325 propagator, i.e., the density of the probability of the displacement distribution law (Callaghan,  
 326 1991; Bacle et al., 2016):

$$327 \quad P(\vec{r}, \Delta \mid \vec{r}_0, 0) = \{4\pi D \Delta\}^{-3/2} \exp \left[ -\frac{(\vec{r} - \vec{r}_0)^2}{4D\Delta} \right] \quad (12)$$

328 where  $\Delta$  is the diffusion time. The self-diffusion propagator that quantifies the mobility along a  
 329 single director is then defined by

$$330 \quad P_\alpha(\vec{r}_\alpha, \Delta \mid \vec{r}_{\alpha 0}, 0) = \{4\pi D_\alpha \Delta\}^{-1/2} \exp \left[ -\frac{(\vec{r}_\alpha - \vec{r}_{\alpha 0})^2}{4D_\alpha \Delta} \right] \quad (13)$$

331 where  $D_\alpha$  is the component of the self-diffusion tensor that describes the mobility of the probe  
 332 along the selected  $\vec{e}_\alpha$  director (Callaghan, 1991).

333 For the BD simulations of water diffusion in Na-kaolinite with only interparticle porosity,  
 334 the same methodology as used by Dabat et al. (2020) was applied. However, in contrast to  
 335 simulations performed in this latter study, the size of the simulation box was not adapted to the  
 336 size of the kaolinite particles. Indeed, in the absence of grain porosity and without consideration  
 337 of specific interfacial effects on the probe dynamics, a mesoscopic simulation is independent  
 338 of the particle size, given that the time step is correctly adapted to the modification of the length  
 339 scale. Accordingly, the same simulation box as for Na-vermiculite (Table S1) was used to

340 compute the water diffusion in the kaolinite samples. Such a consideration is also supported by  
 341 the similar aspect ratios of particles for both types of minerals (0.08 and 0.07 for Na-vermiculite  
 342 and kaolinite, respectively) (Hassan et al., 2005; Reinholdt et al., 2013). For interparticle  
 343 diffusion in a kaolinite sample, a number  $N = 2000$  of water probes with molecular self-  
 344 diffusion  $D_0$  set at  $2.3 \cdot 10^{-9} \text{ m}^2 \text{ s}^{-1}$  were introduced randomly into the interparticle porosity of  
 345 the VPMs. A time step  $\delta t = 200 \text{ ps}$ , over a total simulation time of 0.12 ms, was considered,  
 346 and additional tests showed that smaller values did not provide a difference in the simulation  
 347 results. During the simulations, the collision with the surface of the Na-kaolinite particles was  
 348 treated as a Maxwell's  $A$  wall with the angular probability  $f_A(\theta, f)$  of water probes rebounding  
 349 from the surface given by

$$f_A(\theta, \phi) d\Omega = \cos \theta d\Omega / \pi \quad (14)$$

351 where  $\theta$  and  $f$  are the usual polar and azimuthal angles (with respect to the normal of the surface  
 352 of the particle), and  $d\Omega$  is the element of the solid angle (Fig. 3b). That condition mimics the  
 353 trajectory of a molecule by assuming a residence time at the solid surface that is long enough  
 354 to thermalize its velocity distribution function before being desorbed and returning to the fluid  
 355 (Valleau et al., 1991).

356 For BD simulations of water diffusion in Na-vermiculite, the water probes were allowed  
 357 to diffuse in both the  $\varepsilon_{\text{interp.}}$  and  $\varepsilon_{\text{interl.}}$  porosities. For the interparticle porosity values reported  
 358 in Table S1, the total porosity of the VPM is calculated according to Eq. (1). The self-diffusion  
 359 coefficients for the water molecules in the interlayer space  $D_{\text{interl.}}$  were extracted from previous  
 360 molecular dynamics simulations performed by Tertre et al. (2015) for Na-vermiculite. Although  
 361 these authors only reported the self-diffusion coefficients for  $\text{Na}^+$ , the associated bi-dimensional  
 362 self-diffusion coefficient for the water molecules was found to be at  $D_{\text{interl.}} = 2.3 \cdot 10^{-10} \text{ m}^2 \text{ s}^{-1}$ .  
 363 Such a value is one order of magnitude lower than that of bulk water and is in agreement with  
 364 numerical MD results and experimental quasi-elastic neutron scattering results obtained for

365 tetrahedrally-charged trioctahedral saponite with different layer charges (Michot et al., 2012).  
 366 Note that the obtained  $D_{interl.}$  value is lower than commonly reported for montmorillonite  
 367 (Swenson et al., 2000; Marry and Turq, 2003; Malikova et al., 2005, 2006; Skipper et al., 2006),  
 368 related to the lower charge and location of the charge in the octahedral sheet of this mineral.  
 369 For the initial configuration of the BD simulations, the 2000 water probes were randomly  
 370 introduced in the simulation box with an acceptance probability of 1/3 when the probe was  
 371 included in the solid. The same time step and simulation time as for water diffusion restricted  
 372 to the interparticle porosity only was considered. During the simulation (Fig. 3c), the probes  
 373 colliding with the basal surface of the particles were allowed to rebound according to Eq. (11),  
 374 whereas a specific condition occurred in the case where the probe was in contact with a lateral  
 375 surface. In such a condition, based on a system at equilibrium (Bacle et al., 2016), the probe  
 376 was allowed to penetrate (or leave) the interlayer space of the particle according to the  
 377 acceptance rule:

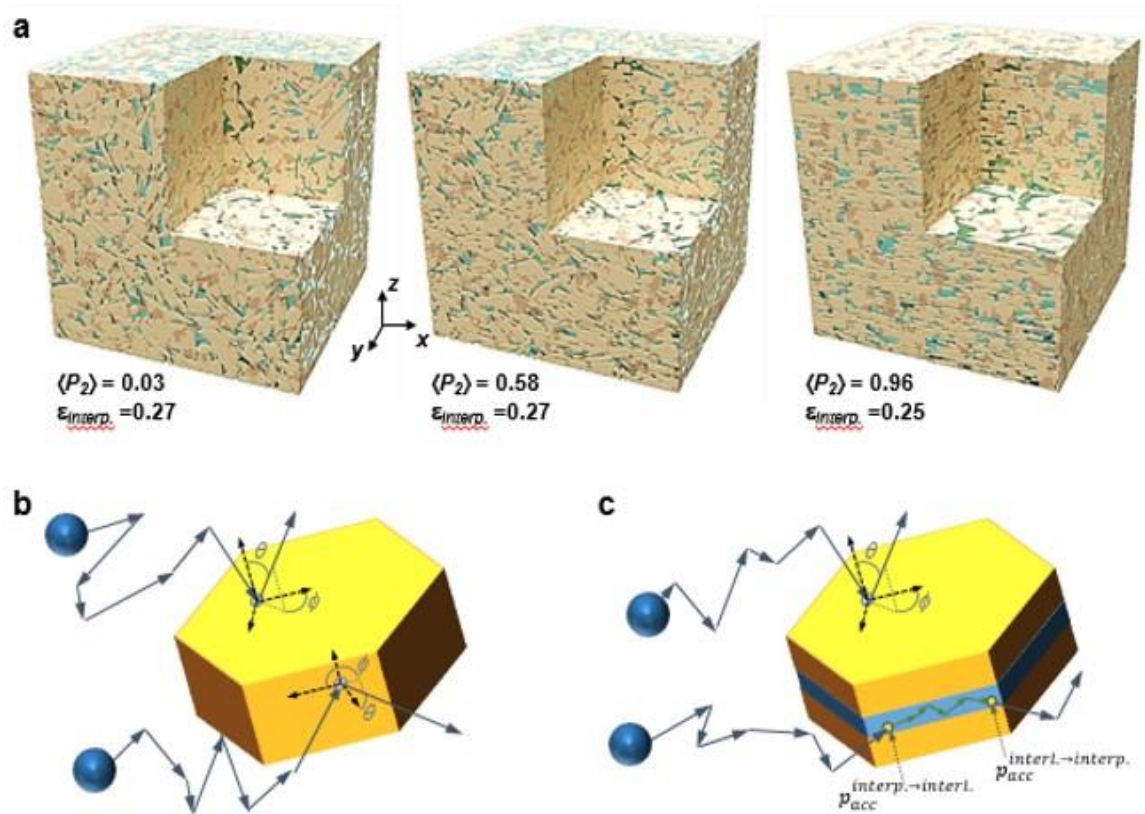
$$378 \quad p_{acc}^{i \rightarrow j} = \min \left[ 1; \frac{p^j}{p^i} \times \frac{p_{gen}^{j \rightarrow i}}{p_{gen}^{i \rightarrow j}} \right] = \min \left[ 1; \frac{c_j}{c_i} \times \left( \frac{D_i}{D_j} \right)^{3/2} \times \exp \left( -\frac{\ell^2}{4D_j \delta t} + \frac{\ell^2}{4D_i \delta t} \right) \right] \quad (18)$$

379 where  $\ell$  is the modulus of the displacement from Eq. (11), and  $c_i$  and  $c_j$  are the water probe  
 380 concentrations in the environments  $i$  and  $j$ , respectively, with self-diffusion coefficients  $D_i$  and  
 381  $D_j$ . In the case of the probe that did not satisfy the acceptance rule to penetrate in the interlayer  
 382 porosity, a rebound was then considered according to Eq. (14) (Fig. 3c).

383 For simulations of water diffusion in both Na-kaolinite and Na-vermiculite, the pore water  
 384 diffusion coefficients  $Dp_\alpha$  along a selected  $\vec{e}_\alpha$  director were extracted from the asymptotic slope  
 385 of the radial mean squared displacement, as follows:

$$386 \quad Dp_\alpha = \lim_{\Delta \rightarrow \infty} \frac{\sum_{i=1}^N (x_{i,\alpha}(0) - x_{i,\alpha}(\Delta))^2}{2N\Delta} \quad (19)$$

387 where  $\alpha$  refers to the single direction  $\vec{e}_\alpha$  on which the mobility is extracted (other parameters  
 388 were already defined above; uncertainty on the calculated  $Dp_\alpha$  values were estimated at 10%).



389

390 **Fig. 3.** (a) Virtual porous media with similar interparticle porosity ( $\epsilon_{\text{interp.}}$ ) values but different anisotropy  
 391 degrees in particle orientation (i.e.,  $\langle P_2 \rangle$  order parameter). (b) Illustration of Brownian dynamics  
 392 displacements of water molecules in an Na-kaolinite sample. Water probes, with a self-diffusion  
 393 coefficient  $D_0$ , diffuse in the interparticle porosity. A rebound of the water probe on a basal or lateral  
 394 surface of the particle is treated according to Maxwell's A wall (see text for details). (c) Brownian  
 395 dynamics of water diffusion in Na-vermiculite. The water probe, initially in the interparticle porosity  
 396 and diffusing with  $D_0$  as the self-diffusion coefficient, can either rebound on the basal surface or  
 397 penetrate the interlayer space of the particle according to the acceptance rule  $p_{\text{acc}}^{\text{interp.} \rightarrow \text{interl.}}$ . If the  
 398 acceptance rule is satisfied, the probe then diffuses in the interlayer space according to the self-diffusion  
 399 coefficient  $D_{\text{interl.}}$ , which was extracted from molecular dynamics. Eventually, the water probe can leave  
 400 the particle and go back to the interparticle porosity according to the acceptance rule  $p_{\text{acc}}^{\text{interl.} \rightarrow \text{interp.}}$ .

401

### 402 3. Results and discussion

#### 403 3.1. Measurement of preferred orientation of clay particles

404 For each sample, longitudinal and transverse 2D-XRS patterns were recorded (Fig. 2b, c)  
 405 with respect to the sample tube axis (i.e., the direction of compaction/preferred orientation of  
 406 clay particles) (Fig. 2a). These patterns are reported in Fig. 4a with their corresponding ODFs  
 407 (Fig. 4b), whereas  $\langle P_2 \rangle$  values extracted from these ODFs are reported in Table 1. For all

408 samples, the transverse ODFs (in gray) remain approximately constant regardless of the  $\theta$  angle  
 409 (Fig. 4b), which indicates that the transverse lamellas are isotropic, as expected for lamellas  
 410 sliced in the direction parallel to the preferred orientation of the clay particles. On the other  
 411 hand, the longitudinal ODFs (in black) display symmetric profiles, which denotes a degree of  
 412 anisotropy in the particles' orientation in this direction.

413 **Table 1.** Experimental results for water tracer (HDO) in Na-kaolinite and Na-vermiculite from through-  
 414 Diffusion (TD) and  $^1\text{H}$  NMR pulsed gradient spin echo (PGSE-NMR) experiments, and the properties  
 415 of the porous media used (material, thickness, porosity, degree in preferred orientation).

|   | Na-kaolinite     | Na-kaolinite     | Na-vermiculite   | Na-vermiculite   |
|---|------------------|------------------|------------------|------------------|
| Preparation method  | Compaction       | Compaction       | Compaction       | Centrifugation   |
| Experimental technique                                    | PGSE-NMR         | TD               | TD               | TD               |
| Sample thick., $L$ (mm)                                   | $10.00 \pm 0.10$ | $6.00 \pm 0.10$  | $7.99 \pm 0.10$  | $6.44 \pm 0.10$  |
| Total porosity, $\varepsilon$                             | $0.26 \pm 0.02$  | $0.26 \pm 0.02$  | $0.49 \pm 0.02$  | $0.49 \pm 0.02$  |
| Interparticle poro., $\varepsilon_{interp.}$              | $0.26 \pm 0.02$  | $0.26 \pm 0.02$  | $0.24 \pm 0.02$  | $0.24 \pm 0.02$  |
| Interlayer poro., $\varepsilon_{interl.}$                 | $0.00 \pm 0.02$  | $0.00 \pm 0.02$  | $0.26 \pm 0.02$  | $0.26 \pm 0.02$  |
| Order parameter, $\langle P_2 \rangle$                    | $0.34 \pm 0.02$  | $0.34 \pm 0.02$  | $0.03 \pm 0.02$  | $0.41 \pm 0.06$  |
| $Dp_z^a$ ( $\times 10^{-10} \text{ m}^2 \text{ s}^{-1}$ ) | 5.77 (5.19-6.35) | 6.92 (5.38-9.23) | 3.61 (3.06-4.49) | 1.82 (1.37-2.27) |
| $De_z^b$ ( $\times 10^{-10} \text{ m}^2 \text{ s}^{-1}$ ) | 1.50 (1.35-1.65) | 1.80 (1.40-2.40) | 1.80 (1.50-2.20) | 0.89 (0.67-1.11) |
| $Dp_z/D_0^c$  | 0.29 (0.26-0.32) | 0.34 (0.26-0.45) | 0.18 (0.15-0.22) | 0.09 (0.07-0.11) |
| $De_z/D_0^d$  | 0.08 (0.07-0.08) | 0.09 (0.07-0.12) | 0.09 (0.07-0.11) | 0.04 (0.03-0.05) |
| $\alpha^e$  | -                | 0.30 (0.25-0.34) | 0.49 (0.40-0.80) | 0.49 (0.40-0.70) |
| $K_d^f$ ( $\text{mL g}^{-1}$ )                            | -                | 0.02 (0.00-0.04) | 0.00 (0.00-0.22) | 0.00 (0.00-0.15) |

<sup>a</sup> Pore diffusion coefficient of water in the direction perpendicular to the preferred orientation of the particles.

<sup>b</sup> Effective diffusion coefficient of water in the direction perpendicular to the preferred orientation of the particles.

<sup>c</sup> Pore diffusion coefficient of water normalized to the self-diffusion coefficient of HDO in bulk water.

<sup>d</sup> Effective diffusion coefficient of water normalized to the self-diffusion coefficient of HDO in bulk water.

<sup>e</sup> Rock capacity factor (see Eq. (S2) in S.D.).

<sup>f</sup> Distribution coefficient (see Eq. (S2) in S.D.).

416 The longitudinal ODF of a Na-kaolinite sample prepared by compaction displays a  
 417 reversed bell-shaped curve, which indicates a main preferred orientation for most of the clay

418 particles in this sample. The corresponding  $\langle P_2 \rangle$  value of  $0.34 \pm 0.025$  was averaged from  
419 several measurement points. For Na-vermiculite samples, the corresponding longitudinal ODFs  
420 display different shapes, as reflected by their contrasted  $\langle P_2 \rangle$  values of  $0.03 \pm 0.025$  and  
421  $0.41 \pm 0.06$  for the compacted and centrifuged samples, respectively. For the purpose of this  
422 study, the contrast in the  $\langle P_2 \rangle$  values between the two samples are sufficient for investigating  
423 the effect of the particles' organization on the diffusion of HDO. Uncertainties on the  $\langle P_2 \rangle$   
424 values were considered to be the standard deviation (STD) of a population of several  
425 measurement points from the same sample.

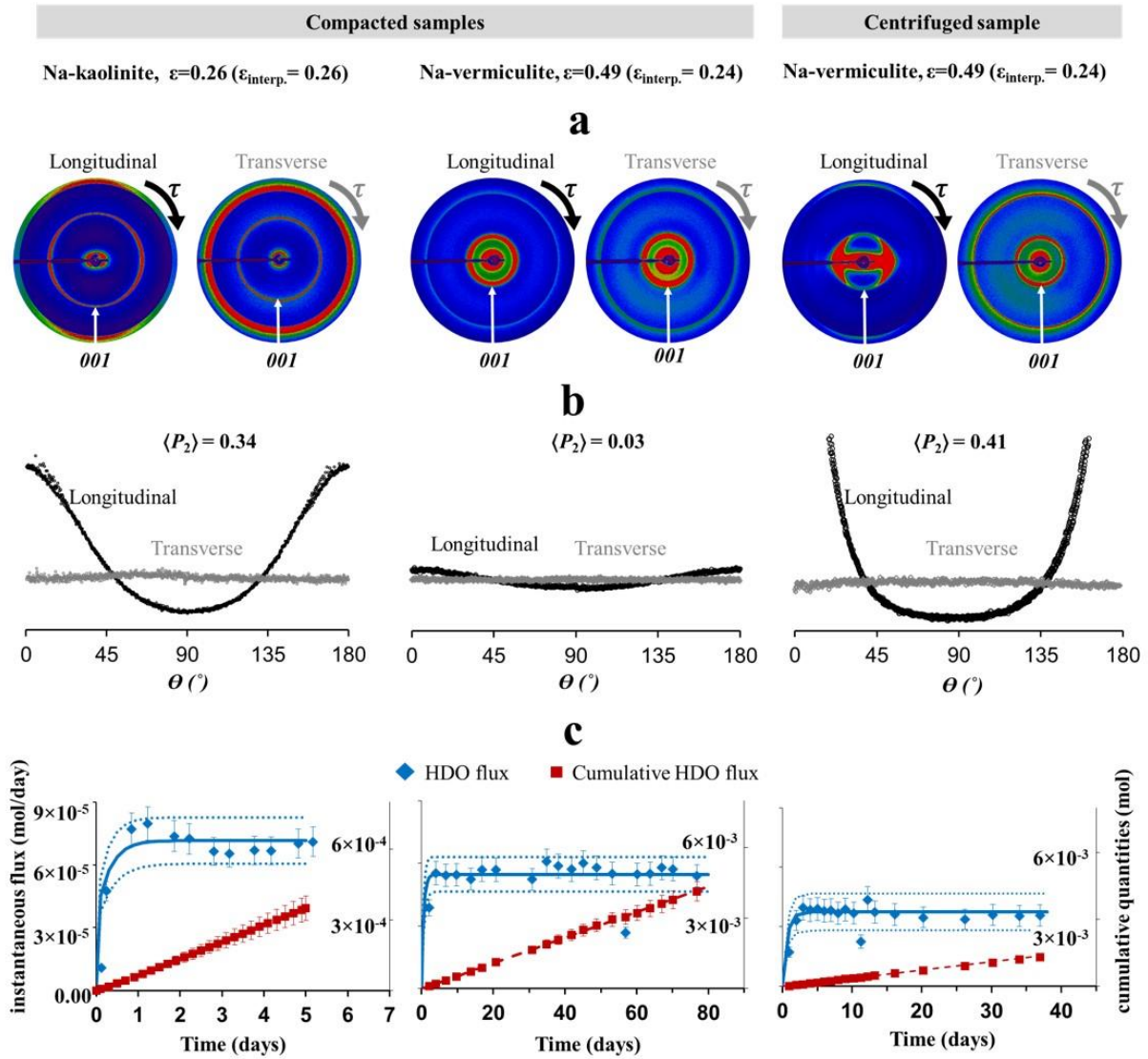
426 The relatively higher uncertainty for the  $\langle P_2 \rangle$  values obtained from the centrifuged sample  
427 with respect to the compacted values ( $\pm 0.06$  and  $\pm 0.025$ , respectively) can be attributed to the  
428 influence of the preparation method (uniaxial compaction vs centrifuging). For example, in the  
429 case of a centrifuged sample, with a slight variation in the solid-solution ratio, hydrostatic or  
430 shear forces, and particles segregation between successive centrifuging cycles led to formation  
431 of successive beds with some heterogeneity in the particles' preferred orientation among them.  
432 Similarly, [Dabat et al. \(2020\)](#) also reported a slightly higher uncertainty for the  $\langle P_2 \rangle$  value of  
433 centrifuged Na-kaolinite samples (i.e., anisotropic) than for the more isotropic values obtained  
434 by compaction.

### 435 **3.2. Water diffusion in Na-kaolinite**

436 The HDO mobility in Na-Kaolinite samples ( $\epsilon = 0.26 \pm 0.025$ ,  $\langle P_2 \rangle = 0.34 \pm 0.02$ ) was  
437 investigated in the direction of the compaction axis (normal to the preferred orientation of clay  
438 particles) with two analytical methods: PGSE-NMR and TD (see [sections 2.4](#)). The results from  
439 both experiments are reported in terms of the pore diffusion coefficient ( $Dp_z$ ) and effective  
440 diffusion coefficient ( $De_z$ ) (definitions in [Section 2.4](#)) in [Table.1](#).

441

442



443 **Fig. 4.** Results from particle orientation and water tracer (HDO) through-diffusion (TD)  
 444 measurements for Na-kaolinite and Na-vermiculite samples. (a) 2D-patterns obtained by X-ray  
 445 scattering technique from longitudinal and transverse lamellas (description in Fig. 2). Color scale ranges  
 446 from light gray to black with increasing scattered intensity. (b) Orientation distribution functions (ODF)  
 447 extracted from an azimuthal scan over 180° along the 001 reflection from longitudinal (black) and  
 448 transverse (gray) lamellas. The intensities are normalized to the same value for comparison. (c)  
 449 Experimental instantaneous flux (black diamonds) and cumulative quantities (gray squares) of HDO  
 450 diffusing through the samples. The solid lines correspond to the fit of the experimental flux, whereas  
 451 dotted lines are simulated flux curves calculated by considering the error range in the diffusion  
 452 parameters (Table 1). Dashed lines correspond to simulated cumulative curves by considering the  
 453 diffusion parameters interpreting the average experimental flux. The scale for the instantaneous flux axis  
 454 is the same for all of the charts.

455 Data reported from Tertre et al. (2018) concerning the instantaneous flux of HDO  
 456 measured in the downstream reservoir during TD experiments in this sample are shown in Fig.  
 457 4c. These data were interpreted with a  $De_z$  equal to  $1.8 (1.4-2.4) \times 10^{-10} \text{ m}^2 \text{ s}^{-1}$  and a rock

458 capacity factor ( $\alpha$ ) value equal to  $\varepsilon$  ( $\alpha = 0.30$  (0.25-0.34) vs.  $\varepsilon = 0.26 \pm 0.02$ ), which allows us  
459 to confirm that HDO is an inert tracer for this sample (i.e., no significant HDO adsorption).

460 Considering the uncertainties associated for each type of measurement ( $\sim 10$  and  $\sim 15\%$   
461 for PGSE-NMR and TD, respectively), both techniques resulted in a similar  $Dp_z$  for HDO in  
462 Na-kaolinite samples (6.9 (5.4-9.2), and  $5.8$  ( $5.2$ - $6.4$ ) $\times 10^{-10}$   $\text{m}^2 \text{s}^{-1}$ , respectively). This similarity  
463 indicates that both techniques, even though they probe very contrasted time scales (days for TD  
464 vs ms for PGSE-NMR), can be used interchangeably to investigate the dynamics of water tracer  
465 in samples composed of non-charged clayey particles irrespective of the differences in the  
466 spatial/temporal scales investigated. Accordingly, the PGSE-NMR method can be used for  
467 upscaling purposes, at least up to the centimeter scale investigated by the TD method.  
468 Moreover, similar  $Dp_z$  values mean that the two samples (the one prepared for PGSE-NMR  
469 analysis in this study and that used by [Tertre et al. \(2018\)](#) for TD experiments) have more or  
470 less the same porosity and degree of anisotropy in their particle orientations (considering the  
471 uncertainties on both parameters).

472 The  $Dp_z/D_0$  values issued from the TD and PGSE-NMR experiments analysis are  
473 compared to those obtained from BD simulations using VPMs ( $\varepsilon = \varepsilon_{\text{interp.}} = 0.25$ - $0.27$ ; see [Table](#)  
474 [S1](#)), which are characterized by different  $\langle P_2 \rangle$  parameter values ([Figure 5a](#)). Overall, the BD  
475 simulations show a decrease in  $Dp_z$  (measured in the direction normal to the preferred  
476 orientation) with the degree of anisotropy of the particles' orientation, in link with the increased  
477 tortuosity of the diffusion pathway. The good agreement between the experimental and  
478 simulated data obtained in this study for an interparticle porosity  $\varepsilon_{\text{interp.}}$  close to 0.25 but also  
479 for a higher porosity value (i.e., 0.5; [Dabat et al. \(2020\)](#)) implies that the different VPMs  
480 generated and characterized by different porosity and particle organizations are well  
481 representative of the real samples, despite the difference in length scales between the real  
482 samples and VPM's ([Ferrage et al., 2015](#)). BD simulations on VPMs can thus be considered a

483 reliable tool to investigate water diffusion in clayey samples, especially in situations that are  
484 experimentally challenging to produce, such as samples that are characterized by different  
485 porosities and a high degree of anisotropy in the particle preferred orientation, since, most often,  
486 the two parameters are coupled (Dabat et al., 2018).

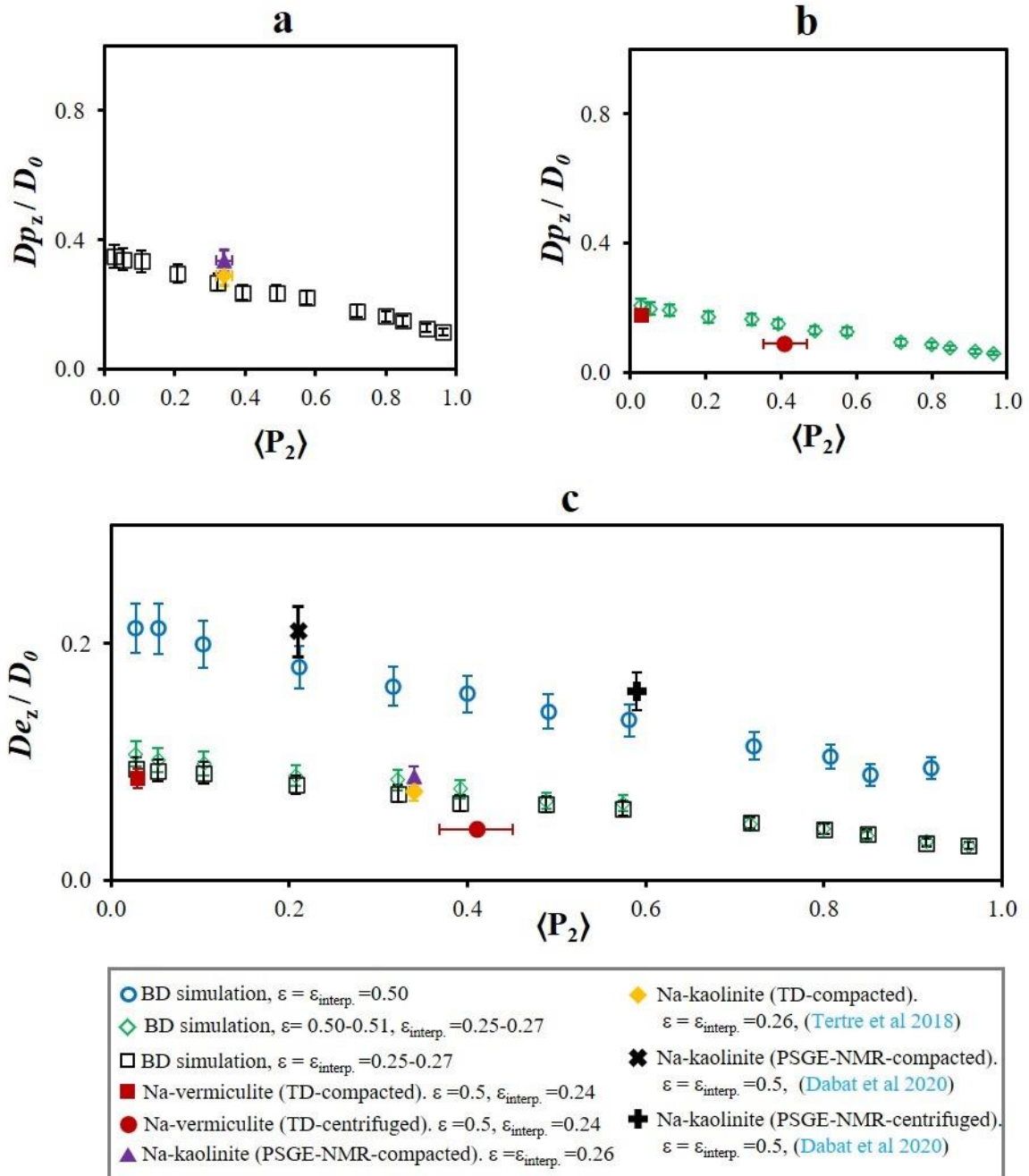
### 487 3.3. Water diffusion in Na-vermiculite

488 TD results obtained with Na-vermiculite samples were fitted with averaged  $\alpha$  values  
489 equal to  $\varepsilon$ , resulting in  $K_d = 0$  (Table 1), which indicates that HDO can be considered an inert  
490 tracer in Na-vermiculite samples, as also reported for kaolinite. However, slight HDO  
491 adsorption cannot be excluded, as suggested by the higher uncertainties obtained on the  
492  $\alpha$  values for Na-vermiculite samples compared to the kaolinite values. Such behavior was also  
493 reported by Tertre et al. (2018) for Na-vermiculite samples and can be attributed to slight HDO  
494 adsorption in the interlayer of Na-vermiculite in relation to its high layer charge.

495 For the same  $\varepsilon$  value ( $\varepsilon = 0.49 \pm 0.025$ ), the contrast in the particles' preferred orientation  
496 (Fig. 4b) between the compacted and centrifuged Na-vermiculite samples ( $\langle P_2 \rangle = 0.03 \pm 0.02$ ,  
497 and  $0.41 \pm 0.06$ , respectively) is well reflected by the difference in their experimental  $Dp_z$   
498 values (Table 1). Indeed, the HDO flux (Fig. 4c) through the compacted sample can be  
499 interpreted with a  $Dp_z$  value equal to  $3.6 (3.0-4.5) \times 10^{-10} \text{ m}^2 \text{ s}^{-1}$ , in comparison to almost two  
500 times lower  $Dp_z$  at  $1.8 (1.4-2.3) \times 10^{-10} \text{ m}^2 \text{ s}^{-1}$  obtained with the centrifuged sample. Such results  
501 indicate that the different Na-vermiculite samples were well-adapted for investigating, with  
502 similar total porosity, the influence of anisotropy in the particles' preferred orientation on the  
503 diffusion of water in a charged/dual porosity clayey media. Moreover, the data also infer that  
504 in a clayey media, and together with porosity, the preferred orientation of the particles acts as  
505 a first-order parameter in the control of the water diffusion. This behavior, previously reported  
506 by Dabat et al. (2020) for non-charged clayey samples (i.e., Na-kaolinite), therefore also  
507 extends to the case of charged clayey samples with a dual porosity. These findings decisively

508 show that comprehensive data on the orientation of the particles in a clay-rich media is a  
509 prerequisite to correctly predict water diffusion within it. Finally, all the above stresses the need  
510 to develop diffusion models in which both the porosity and the degree of particle preferred  
511 orientation are explicitly included to increase the predictive capacity of such models.

512 In Fig. 5b and similar to Na-kaolinite samples, a good agreement is observed between  
513 experimental points from Na-vermiculite samples and simulated data ( $\varepsilon = 0.50-0.51$  and  
514  $\varepsilon_{\text{interp.}} = 0.25-0.27$ ; Table S1). Moreover, despite the higher  $\varepsilon$  value for Na-vermiculite  
515 compared to Na-kaolinite, the lower  $Dp_z$  values obtained for Na-vermiculite clearly highlight  
516 the role played by the interlayer porosity on the overall reduced mobility of the water molecules  
517 in the vicinity of charged clay particles (Nakashima and Mitsumori, 2005; Michot et al., 2012;  
518 Porion et al., 2014). Note that in Fig. 5b, the point obtained for the centrifuged Na-vermiculite  
519 sample at  $\langle P_2 \rangle = 0.41$  is somewhat lower than the corresponding simulated point. Such small  
520 aberration can be due to the slightly lower interparticle porosity in the case of the experimental  
521 Na-vermiculite sample ( $\varepsilon_{\text{interp.}} = 0.24$ ) compared to that used for the BD simulation  
522 ( $\varepsilon_{\text{interp.}} = 0.25-0.27$ ). In addition, one can consider that due to the increased heterogeneity for the  
523 centrifuged sample, which is characterized by the wider variation in  $\langle P_2 \rangle$  values, water diffusion  
524 could be controlled by zones in the samples with higher  $\langle P_2 \rangle$  values and not by the mean degree  
525 of preferred orientation. Despite this marginal difference, the good agreement between the  
526 experimental and calculated  $Dp_z$  values can be assigned to the lack of osmotic swelling in the  
527 Na-vermiculite sample, which allows a correct quantitative description of the different types of  
528 porosities volumes. In this respect, BD simulations on such granular virtual systems can be  
529 considered to be a useful tool for investigating the role played by different parameters (i.e.,  
530 porosity, orientation of particles, and dual porosity volumes) on the overall diffusion process  
531 of water in Na-vermiculite dual porosity media.



532 **Figure 5.** Comparison between experimental and Brownian dynamics (BD) simulated water diffusion  
533 coefficients in the direction perpendicular to the preferred orientation of clay particles as a function of  
534 order parameter  $\langle P_2 \rangle$  values. All diffusion coefficients are normalized to the self-diffusion coefficient of  
535 HDO in bulk water ( $D_0$ ). (a) Pore diffusion coefficients ( $D_{p_z}/D_0$ ) of water in Na-kaolinite. Experimental  
536 data are shown in filled symbols (triangle and diamond for  $^1\text{H}$  NMR Pulsed Gradient Spin Echo (PGSE-  
537 NMR) and through-diffusion (TD) methods, respectively), whereas simulated data are shown as non-  
538 filled squares. (b) Pore diffusion coefficients ( $D_{p_z}/D_0$ ) of water in Na-vermiculite. Experimental data  
539 are shown in filled symbols (circle and square for the centrifuged and compacted samples, respectively),  
540 whereas simulated data are shown as non-filled diamonds. (c) Summary of (a) and (b) displayed as  
541 effective diffusion coefficients ( $De_z/D_0$ ). Data are also compared to experimental (+ and × symbols) and  
542 simulated (non-filled circles) results from Dabat et al. (2020).

543

544 **3.4. The influence of interlayer vs. interparticle porosities on HDO diffusion in clayey**  
545 **samples**

546 To assess the role played by the two porosities types (interlayer and interparticle), the  
547 HDO diffusivity is discussed below in terms of  $De_z$  since this parameter is commonly used over  
548  $Dp_z$  in macroscopic models to describe the diffusing flux traversing a sample (Bourg and  
549 Tournassat, 2015; Tournassat and Steefel, 2019 and references therein). The obtained  $De_z$   
550 values for water, normalized to self-diffusion in bulk  $D_0$ , measured for both materials (kaolinite  
551 and Na-vermiculite) using the two techniques (PSGE-NMR and TD), are plotted in Fig. 5c as  
552 a function of the  $\langle P_2 \rangle$  parameter. These data are compared to the calculated ones obtained from  
553 BD simulations assuming that all porosity is accessible to diffusion (as confirmed by HDO  
554 alpha values previously discussed and reported in Table 1). Considering that experimental  
555 samples composed of Na-vermiculite and Na-kaolinite particles have approximatively the same  
556 interparticle porosity (i.e., 0.26 vs. 0.24 for kaolinite and vermiculite, respectively) and that all  
557 of the porosity of the Na-vermiculite samples is accessible to water diffusion, one can expect  
558 that  $De_z$  obtained with Na-vermiculite samples are intermediate between those simulated for  
559  $\varepsilon_{\text{interp.}} = 0.25$  and  $\varepsilon_{\text{interp.}} = 0.5$  (for similar  $\langle P_2 \rangle$  values). In fact, experimental data obtained with  
560 Na-vermiculite ( $\varepsilon = 0.49$ ) are drastically much closer to those simulated at  $\varepsilon_{\text{interp.}} = 0.25$  than to  
561 those simulated at  $\varepsilon_{\text{interp.}} = 0.5$  (Fig. 5c). Such behavior suggests that even though interlayer  
562 porosity is available for diffusion, the contribution of the flux of HDO diffusing in this  
563 interlayer volume is very marginal compared to that in the interparticle porosity, which results  
564 in  $De_z$  values that are almost independent of the interlayer porosity of the material. Interestingly,  
565 the evolution of the diffusion anisotropy ratios  $\frac{De_{xy}}{De_z}$  with the  $\langle P_2 \rangle$  values reported in Fig. 6  
566 indicates a significant increase in anisotropy with the increased degree of preferred orientation  
567 of particles. This behavior is the same for different values of the total porosity and different

568 distributions between interparticle or interlayer volumes. This finding implies that the  
 569 anisotropy of water diffusion can be, for the range of porosity investigated, directly linked to  
 570 the  $\langle P_2 \rangle$  parameter, irrespective of the porosity value or distribution. The limited contribution  
 571 of interlayer porosity on the diffusive flux crossing a sample, reported in this study by coupling  
 572 BD simulations with experimental results obtained with both Na-vermiculite and Na-kaolinite  
 573 samples, is in agreement with the results reported by [Churakov and Gimmi. \(2011\)](#). Based on  
 574 molecular dynamics and random walk simulations, these authors showed that the proportion of  
 575 interlayer porosity (and associated diffusion) in the total porosity of virtual porous media has  
 576 only a minor influence on the water diffusion. Note that the dominant role played by the  
 577 interparticle porosity was already qualitatively addressed by [Tertre et al. \(2018\)](#) to explain the  
 578 difference between experimental TD data obtained for Na-vermiculite and Na-kaolinite  
 579 samples. However, although the porosity distribution (i.e.,  $\varepsilon_{\text{interl.}}$  and  $\varepsilon_{\text{interp.}}$ ) was known in their  
 580 Na-vermiculite samples, the particle organization in these samples was not quantified,  
 581 rendering it impossible to decouple the role played by each one of these variables on the global  
 582 diffusion process.

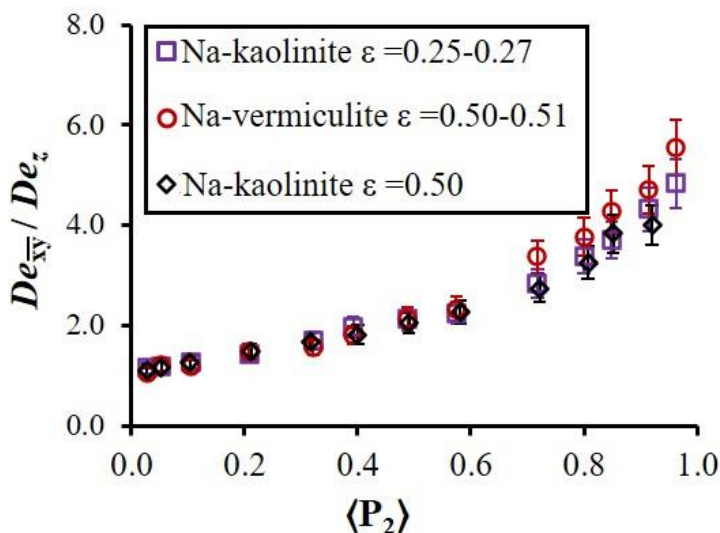


**Fig. 6.** Influence of porosity and its distribution between interlayer and interparticle volumes on the evolution of the diffusion anisotropy ratio  $De_{\overline{xy}}/De_z$  as a function of the order parameter  $\langle P_2 \rangle$ . The anisotropy ratio is calculated based on the BD simulated mean effective water diffusion coefficients in the (x,y)

591 plane ( $De_{\overline{xy}}$ ) over the z direction ( $De_z$ ) with respect to the direction of the preferred orientation of the  
 592 clay particles. Data are shown for Na-kaolinite with  $\varepsilon = 0.25$  (squares, this study) or  $\varepsilon = 0.50$  (diamonds,  
 593 [Dabat et al. \(2020\)](#)), and for Na-vermiculite with  $\varepsilon = 0.50-0.51$  and  $\varepsilon_{\text{interp.}} = 0.25-0.27$  (circles, this study).

594 Furthermore, as previously discussed in the introduction, determination of the  $\varepsilon_{\text{interl.}}/\varepsilon_{\text{interp.}}$   
595 value is not easy for smectite due to osmotic swelling of this mineral, especially when the  
596 saturating cations are  $\text{Na}^+$ , which makes it difficult to discriminate the role played by interlayer  
597 and interparticle porosities on the global diffusivity of water tracer in this mineral. Such a  
598 phenomenon was, to some extent, indicated by [Melkior et al. \(2009\)](#), who reported that the  
599 effective diffusion coefficient of water tracer was significantly dependent on the nature of the  
600 compensating cations in samples made of smectitic particles (for the same total porosity), with  
601  $De_z$  increasing from Na-smectite, Ca-smectite to Cs-smectite. These authors attributed this  
602 variation to the absence of gel formation for the Cs-samples compared to the Na-samples (and  
603 to a lesser extent in Ca-samples). This observation was most likely related to the difficulty of  
604 considering a defined interparticle porosity (i.e., pores not submitted to the particle charge) for  
605 Na-smectites compared to Cs ones, and consequently raises the question about the relevance of  
606 considering the  $De_z$  values obtained with Na-smectites as reference data for models describing  
607 dual porosity clayey system. In that regard, the experimental results obtained in this study with  
608 Na-vermiculite samples represent a new set of data for an extensive validation of dual-porosity  
609 reactive transport models.

#### 610 **4. Concluding remarks and perspectives**

611 A methodology was developed in this study to prepare experimental clayey samples for  
612 which the porosity distribution (interlayer ( $\varepsilon_{\text{interl.}}$ )/interparticle ( $\varepsilon_{\text{interp.}}$ )) and particle organization  
613 can be controlled independently. These new procedures were successfully applied to prepare  
614 samples characterized by the same interparticle porosity but with the presence or not of  
615 interlayer porosity accessible to water diffusion (Na-kaolinite vs Na-vermiculite samples), used  
616 to investigate the role played by the two types of porosities and the particle organization on the  
617 global diffusion of water.

618 The similarity of the diffusion data obtained for Na-kaolinite by two independent  
619 experimental techniques (i.e., Pulsed Gradient Spin Echo attenuation measurements by Nuclear  
620 Magnetic Resonance (PGSE-NMR) and through-diffusion (TD)) probing different length and  
621 time scales (i.e., ms for PGSE-NMR *vs.* several days for TD), shows that a representative  
622 elementary volume for the analysis of water diffusion process in clayey materials was reached  
623 with PGSE-NMR method. Moreover, these two experimental techniques are found to be very  
624 complementary for the analysis of water diffusion in clayey media. On the one hand, PGSE-  
625 NMR allows obtaining the full tensor of the water diffusion on the same sample, whereas the  
626 TD experiments must be repeated when changing the probed direction of diffusion. On the other  
627 hand, PGSE-NMR cannot be used when the sample contains a very high quantity of  
628 paramagnetic elements, such as Fe in the Na-vermiculite used in this study, or when the probe  
629 confinement is high (the case of water molecule in the interlayer of Na-vermiculite as a result  
630 of its high structural charge). In that regard TD can be advantageously used irrespective of the  
631 chemical composition of the sample and interlayer probe confinement.

632 By accounting for the uncertainties in both the porosity and particle organization  
633 measurements, there were good agreements between the effective diffusion coefficients derived  
634 from the experimental measurements obtained for all samples and simulated data. This finding  
635 showed that, in a dual-porosity clayey media, even though the interlayer is accessible to water  
636 diffusion, interparticle porosity and preferential orientation of the particles act as first-order  
637 parameters in the global flux of water diffusing through these media, at least for the range of  
638 porosity investigated. These results were obtained irrespective of the directional diffusion  
639 probed, and they allowed us to conclude that the  $\langle P_2 \rangle$  parameter (i.e., mathematical function  
640 derived from two-dimensional X-Ray Scattering measurements comprised between 0 for an  
641 isotropic particle organization and 1 for a perfectly anisotropic organization) is an excellent

642 descriptor of the anisotropy of the diffusion of water in materials made of swelling clay  
643 particles.

644 Due to osmotic swelling of montmorillonite clay minerals, especially when the charge  
645 compensating cation is  $\text{Na}^+$ , distribution of interparticle and interlayer porosities is extremely  
646 difficult to be determined. As logical continuation of this work, Na-vermiculite samples  
647 characterized by well-defined  $\varepsilon_{\text{interl.}}/\varepsilon_{\text{interp.}}$  ratios and particle organization, can be used for  
648 further investigating the link between geometrical properties and the diffusion of charged  
649 (ionic) tracers in swelling clays. Such approach would likely provide key information for  
650 decoupling the role played by interfacial charges located on either basal or edge surfaces of Na-  
651 vermiculite from other parameters linked to the geometric organization of the particles, such as  
652 the preferential orientation of the clay particles or the different porosities accessible to diffusion.

### 653 **Acknowledgments**

654 The results presented are part of the Ph.D. thesis of A.A. granted by “Région Nouvelle-  
655 Aquitaine”, University of Poitiers, France. Stephan Rouzière (LPS, Saclay, France) is  
656 acknowledged for technical assistance in the XRS measurements. Dr. Jerome Labanowski  
657 (IC2MP, Poitiers, France) is thanked for providing access to the lyophilizer used in this study.  
658 Claude Veit (IC2MP, Poitiers, France) is thanked for the design and conception of the  
659 compaction and centrifugation cells for the sample preparation. The authors are grateful to the  
660 CNRS interdisciplinary “défi Needs” through its “MiPor” program (Project DARIUS), the  
661 H2020 European program EURAD through its “Future” WP, the French government program  
662 “Investissements d’Avenir” (EUR INTREE, reference ANR-18-EURE-0010), and the  
663 European Union (ERDF) and “Région Nouvelle Aquitaine” for providing financial support for  
664 this study.

665

666

667 **5. References**

- 668 Abend, S., Lagaly, G., 2000. Sol–gel transitions of sodium montmorillonite dispersions.  
669 Applied Clay Science 16, 201–227. [https://doi.org/10.1016/S0169-1317\(99\)00040-X](https://doi.org/10.1016/S0169-1317(99)00040-X)
- 670 Altmann, S., Aertsens, M., Appelo, T., Bruggeman, C., Gaboreau, S., Glaus, M., Jacquier, P.,  
671 Kupcik, T., Maes, N., Montoya, V., Rabung, T., Savoye, S., et al, 2015. Processes of  
672 cation migration in clayrocks: Final Scientific Report of the CatClay European Project.  
673 CEA.
- 674 Andra, 2005. Argile : Évaluation de la Faisabilité du Stockage Géologique en Formation  
675 Argileuse. Document du Synthèse, Andra.
- 676 Arguelles, A., Leoni, M., Blanco, J.A., Marcos, C., 2010. Semi-ordered crystalline structure  
677 of the Santa Olalla vermiculite inferred from X-ray powder diffraction. American  
678 Mineralogist 95, 126–134. <https://doi.org/10.2138/am.2010.3249>
- 679 Bachu, S., 2008. CO<sub>2</sub> storage in geological media: Role, means, status and barriers to  
680 deployment. Progress in Energy and Combustion Science 34, 254–273.  
681 <https://doi.org/10.1016/j.pecs.2007.10.001>
- 682 Bacle, P., Dufrêche, J.-F., Rotenberg, B., Bourg, I.C., Marry, V., 2016. Modeling the  
683 transport of water and ionic tracers in a micrometric clay sample. Applied Clay  
684 Science 123, 18–28. <https://doi.org/10.1016/j.clay.2015.12.014>
- 685 Bear, J., 1972. Dynamics of Fluids in Porous Media. Dover Publication, New York.
- 686 Bestel, M., 2014. Water–montmorillonite systems: Neutron scattering and tracer through-  
687 diffusion studies (Thesis). University of Bern, Bern-Switzerland.
- 688 Bestel, M., Glaus, M.A., Frick, S., Gimmi, T., Juranyi, F., Van Loon, L.R., Diamond, L.W.,  
689 2018. Combined tracer through-diffusion of HTO and <sup>22</sup>Na through Na-  
690 montmorillonite with different bulk dry densities. Applied Geochemistry 93, 158–166.  
691 <https://doi.org/10.1016/j.apgeochem.2018.04.008>
- 692 Bennett, R.H., Brya, W.R., Keller, G.H., 1981. Clay fabric of selected submarine sediments;  
693 fundamental properties and models. Journal of Sedimentary Research 51, 217–232.  
694 <https://doi.org/10.1306/212F7C52-2B24-11D7-8648000102C1865D>
- 695 Bourg, I.C., Bourg, A.C.M., Sposito, G., 2003. Modeling diffusion and adsorption in  
696 compacted bentonite: a critical review. Journal of Contaminant Hydrology 61, 293–  
697 302. [https://doi.org/10.1016/S0169-7722\(02\)00128-6](https://doi.org/10.1016/S0169-7722(02)00128-6)
- 698 Bourg, I.C., Sposito, G., Bourg, A.C.M., 2006. Tracer diffusion in compacted, water-saturated  
699 bentonite. Clays Clay Miner. 54, 363–374.  
700 <https://doi.org/10.1346/CCMN.2006.0540307>
- 701 Bourg, I.C., Tournassat, C., 2015. Self-Diffusion of Water and Ions in Clay Barriers, in:  
702 Developments in Clay Science. Elsevier, pp. 189–226. <https://doi.org/10.1016/B978-0-08-100027-4.00006-1>
- 703
- 704 Callaghan, P.T., 1991. Principles of nuclear magnetic resonance microscopy. Clarendon  
705 Press.
- 706 Charlet, L., Alt-Epping, P., Wersin, P., Gilbert, B., 2017. Diffusive transport and reaction in  
707 clay rocks: A storage (nuclear waste, CO<sub>2</sub>, H<sub>2</sub>), energy (shale gas) and water quality  
708 issue. Advances in Water Resources 106, 39–59.  
709 <https://doi.org/10.1016/j.advwatres.2017.03.019>
- 710 Churakov, S.V., Gimmi, T., 2011. Up-Scaling of Molecular Diffusion Coefficients in Clays:  
711 A Two-Step Approach. J. Phys. Chem. C 115, 6703–6714.  
712 <https://doi.org/10.1021/jp112325n>

- 713 Dabat, T., Hubert, F., Paineau, E., Launois, P., Laforest, C., Grégoire, B., Dazas, B., Tertre,  
714 E., Delville, A., Ferrage, E., 2019. A general orientation distribution function for clay-  
715 rich media. *Nat Commun* 10, 5456. <https://doi.org/10.1038/s41467-019-13401-0>
- 716 Dabat, T., Mazurier, A., Hubert, F., Tertre, E., Grégoire, B., Dazas, B., Ferrage, E., 2018.  
717 Mesoscale Anisotropy in Porous Media Made of Clay Minerals. A Numerical Study  
718 Constrained by Experimental Data. *Materials* 11, 1972.  
719 <https://doi.org/10.3390/ma11101972>
- 720 Dabat, T., Porion, P., Hubert, F., Paineau, E., Dazas, B., Grégoire, B., Tertre, E., Delville, A.,  
721 Ferrage, E., 2020. Influence of preferred orientation of clay particles on the diffusion  
722 of water in kaolinite porous media at constant porosity. *Applied Clay Science* 184,  
723 105354. <https://doi.org/10.1016/j.clay.2019.105354>
- 724 Dagnelie, R.V.H., Arnoux, P., Enaux, J., Radwan, J., Ner, P., 2017. Perturbation induced by a  
725 nitrate plume on diffusion of solutes in a large-scale clay rock sample. *Applied Clay*  
726 *Science* 141. 219-226.
- 727 Dagnelie, R.V.H., Rasamimanana, S., Blin, V., Radwan, J., Thory, E., Robinet, J.-C., Lefèvre,  
728 G., 2018. Diffusion of organic anions in clay-rich media: Retardation and effect of  
729 anion exclusion. *Chemosphere* 213, 472–480.  
730 <https://doi.org/10.1016/j.chemosphere.2018.09.064>
- 731 De La Calle, C., Pezerat, H., Gasperin, M., 1977. Problemes d'ordre-désordre dans les  
732 vermiculites structure du minéral calcique hydraté a 2 couches. *Journal de Physique*  
733 38, 128–133.
- 734 Durrieu, J., Argillier, J.F., Rosenberg, E., Li, Y., 1997. Static and Dynamic Filtration  
735 Properties of Aqueous Suspensions of Clays and Electrolytes. *Rev. Inst. Fr. Pét.* 52,  
736 207–218. <https://doi.org/10.2516/ogst:1997020>
- 737 Dykhuizen, R.C., Casey, W.H., 1989. An analysis of solute diffusion in rocks. *Geochimica et*  
738 *Cosmochimica Acta* 53, 2797–2805. [https://doi.org/10.1016/0016-7037\(89\)90157-9](https://doi.org/10.1016/0016-7037(89)90157-9)
- 739 Farver, J.R., Yund, R.A., 1999. Oxygen bulk diffusion measurements and TEM  
740 characterization of a natural ultramylonite: implications for fluid transport in mica-  
741 bearing rocks. *J. Metamorph. Geol* 17, 669–683.
- 742 Faurel, M., 2012. Conception et mise en place d'expériences de diffusion de l'eau et de  
743 solutés dans des milieux poreux modèles d'argiles gonflantes. Université de Poitiers,  
744 Poitiers, France.
- 745 Ferrage, E., Hubert, F., Baronnet, A., Grauby, O., Tertre, E., Delville, A., Bihannic, I., Prêt,  
746 D., Michot, L.J., Levitz, P., 2018. Influence of crystal structure defects on the small-  
747 angle neutron scattering/diffraction patterns of clay-rich porous media. *J Appl*  
748 *Crystallogr* 51, 1311–1322. <https://doi.org/10.1107/S160057671801052X>
- 749 Ferrage, E., Hubert, F., Tertre, E., Delville, A., Michot, L.J., Levitz, P., 2015. Modeling the  
750 arrangement of particles in natural swelling-clay porous media using three-  
751 dimensional packing of elliptic disks. *Physical Review E* 91, 062210.  
752 <https://doi.org/10.1103/PhysRevE.91.062210>
- 753 García-Gutiérrez, M., Cormenzana, J.L., Missana, T., Mingarro, M., Martín, P.L., 2006.  
754 Large-scale laboratory diffusion experiments in clay rocks. *Physics and Chemistry of*  
755 *the Earth, Parts A/B/C* 31, 523–530. <https://doi.org/10.1016/j.pce.2006.04.004>
- 756 Gieseking, J.E. (Ed.), 1975. *Soil Components Vol. 2: Inorganic Components*, 1st ed. Springer-  
757 Verlag Berlin Heidelberg.
- 758 Gimmi, T., Churakov, S.V., 2019. Water retention and diffusion in unsaturated clays:  
759 Connecting atomistic and pore scale simulations. *Applied Clay Science* 175, 169–183.  
760 <https://doi.org/10.1016/j.clay.2019.03.035>

761 Gimmi, T., Kosakowski, G., 2011. How Mobile Are Sorbed Cations in Clays and Clay  
762 Rocks? *Environ. Sci. Technol.* 45, 1443–1449. <https://doi.org/10.1021/es1027794>

763 Glaus, M.A., Frick, S., Rossé, R., Loon, L.R.V., 2010. Comparative study of tracer diffusion  
764 of HTO,  $^{22}\text{Na}^+$  and  $^{36}\text{Cl}^-$  in compacted kaolinite, illite and montmorillonite.  
765 *Geochimica et Cosmochimica Acta* 74, 1999–2010.  
766 <https://doi.org/10.1016/j.gca.2010.01.010>

767 González García, F., García Ramos, G., 1960. On the genesis and transformation of  
768 vermiculite. Presented at the Transactions 7th int. Congr. Soil Sci., Spain, pp. 482–  
769 491.

770 González Sánchez, F., Jurányi, F., Gimmi, T., Van Loon, L., Unruh, T., Diamond, L.W.,  
771 2008a. Translational diffusion of water and its dependence on temperature in charged  
772 and uncharged clays: A neutron scattering study. *J. Chem. Phys.* 129, 174706.  
773 <https://doi.org/10.1063/1.3000638>

774 González Sánchez, F., Van Loon, L.R., Gimmi, T., Jakob, A., Glaus, M.A., Diamond, L.W.,  
775 2008b. Self-diffusion of water and its dependence on temperature and ionic strength in  
776 highly compacted montmorillonite, illite and kaolinite. *Applied Geochemistry* 23,  
777 3840–3851. <https://doi.org/10.1016/j.apgeochem.2008.08.008>

778 Gunsteren, W.F., Berendsen, H.J.C., Rullmann, J.A.C., 1981. Stochastic dynamics for  
779 molecules with constraints. *Molecular Physics* 44, 69–95.  
780 <https://doi.org/10.1080/00268978100102291>

781 Hassan, M.S., Villieras, F., Gaboriaud, F., Razafitianamaharavo, A., 2005. AFM and low-  
782 pressure argon adsorption analysis of geometrical properties of phyllosilicates. *Journal*  
783 *of Colloid and Interface Science* 296, 614–623.  
784 <https://doi.org/10.1016/j.jcis.2005.09.028>

785 Hermans, P.H., Platzek, P., 1939. Beiträge zur Kenntnis des Deformationsmechanismus und  
786 der Feinstruktur der Hydratzellulose. *Kolloid-Z, Kolloid-Z* 88, 68–72.

787 Jacobs, E., Aertsens, M., Maes, N., Bruggeman, C., Swennen, R., Krooss, B., Amann-  
788 Hildenbrand, A., Littke, R., 2017. The Dependency of Diffusion Coefficients and  
789 Geometric Factor on the Size of the Diffusing Molecule: Observations for Different  
790 Clay-Based Materials. *Geofluids* 2017, 1–16. <https://doi.org/10.1155/2017/8652560>

791 Landais, P., 2006. Advances in geochemical research for the underground disposal of high-  
792 level, long-lived radioactive waste in a clay formation. *Journal of Geochemical*  
793 *Exploration* 88, 32–36. <https://doi.org/10.1016/j.gexplo.2005.08.011>

794 Liu, L., 2013. Prediction of swelling pressures of different types of bentonite in dilute  
795 solutions. *Colloids and Surfaces A: Physicochemical and Engineering Aspects* 434,  
796 303–318. <https://doi.org/10.1016/j.colsurfa.2013.05.068>

797 Loeber, L., 1992. Etude de la structure des cakes d'argile formés sur la paroi des puits au  
798 cours du forage. Université d'Orléans, Orléans-France.

799 Malikova, N., Cadène, A., Marry, V., Dubois, E., Turq, P., Zanotti, J.-M., Longeville, S.,  
800 2005. Diffusion of water in clays – microscopic simulation and neutron scattering.  
801 *Chemical Physics* 317, 226–235. <https://doi.org/10.1016/j.chemphys.2005.04.035>

802 Malikova, N., Cadène, A., Marry, V., Dubois, E., Turq, P., 2006. Diffusion of Water in Clays  
803 on the Microscopic Scale: Modeling and Experiment. *J. Phys. Chem. B* 110, 3206–  
804 3214. <https://doi.org/10.1021/jp056954z>

805 Marcos, C., Argüelles, A., Ruíz-Conde, A., P. J. Sánchez-Soto, Blanco, J.A., 2003. Study of  
806 the dehydration process of vermiculites by applying a vacuum pressure: formation of  
807 interstratified phases. *Mineral. mag.* 67, 1253–1268.  
808 <https://doi.org/10.1180/0026461036760163>

809 Marry, V., Turq, P., Cartailier, T., Levesque, D., 2002. Microscopic simulation of structure  
810 and dynamics of water and counterions in a monohydrated montmorillonite. *The*  
811 *Journal of Chemical Physics* 117, 3454–3463. <https://doi.org/10.1063/1.1493186>  
812 Marry, V., Turq, P., 2003. Microscopic Simulations of Interlayer Structure and Dynamics in  
813 Bihydrated Heteroionic Montmorillonites. *J. Phys. Chem. B* 107, 1832–1839.

814 Melkior, T., Gaucher, E.C., Brouard, C., Yahiaoui, S., Thoby, D., Clinard, Ch., Ferrage, E.,  
815 Guyonnet, D., Tournassat, C., Coelho, D., 2009. Na<sup>+</sup> and HTO diffusion in compacted  
816 bentonite: Effect of surface chemistry and related texture. *Journal of Hydrology* 370,  
817 9–20. <https://doi.org/10.1016/j.jhydrol.2009.02.035>  
818 Mermut, A.R., Cano, A.F., 2001. Baseline Studies of the Clay Minerals Society Source Clays:  
819 Chemical Analyses of Major Elements. *Clays and Clay Minerals* 49, 381–386.  
820 <https://doi.org/10.1346/CCMN.2001.0490504>  
821 Michot, L.J., Ferrage, E., Jiménez-Ruiz, M., Boehm, M., Delville, A., 2012. Anisotropic  
822 Features of Water and Ion Dynamics in Synthetic Na- and Ca-Smectites with  
823 Tetrahedral Layer Charge. A Combined Quasi-elastic Neutron-Scattering and  
824 Molecular Dynamics Simulations Study. *J. Phys. Chem. C* 116, 16619–16633.  
825 <https://doi.org/10.1021/jp304715m>  
826 Nakashima, Y., Mitsumori, F., 2005. H<sub>2</sub>O self-diffusion restricted by clay platelets with  
827 immobilized bound H<sub>2</sub>O layers: PGSE NMR study of water-rich saponite gels.  
828 *Applied Clay Science* 28, 209–221. <https://doi.org/10.1016/j.clay.2004.01.017>  
829 Ochs, M., Lothenbach, B., Wanner, H., Sato, H., Yui, M., 2001. An integrated sorption–  
830 diffusion model for the calculation of consistent distribution and diffusion coefficients  
831 in compacted bentonite. *Journal of Contaminant Hydrology* 47, 283–296.  
832 [https://doi.org/10.1016/S0169-7722\(00\)00157-1](https://doi.org/10.1016/S0169-7722(00)00157-1)  
833 Porion, P., Faugère, A.M., Delville, A., 2014. Structural and Dynamical Properties of Water  
834 Molecules Confined within Clay Sediments Probed by Deuterium NMR Spectroscopy,  
835 Multiquanta Relaxometry, and Two-Time Stimulated Echo Attenuation. *J. Phys.*  
836 *Chem. C* 118, 20429–20444. <https://doi.org/10.1021/jp506312q>  
837 Porion, P., Ferrage, E., Hubert, F., Tertre, E., Dabat, T., Faugère, A.M., Condé, F., Warmont,  
838 F., Delville, A., 2018. Water Mobility within Compacted Clay Samples: Multi-Scale  
839 Analysis Exploiting <sup>1</sup>H NMR Pulsed Gradient Spin Echo and Magnetic Resonance  
840 Imaging of Water Density Profiles. *ACS Omega* 3, 7399–7406.  
841 <https://doi.org/10.1021/acsomega.8b01083>  
842 Pret, D., 2003. Nouvelles méthodes quantitatives de cartographie de la minéralogie et de la  
843 porosité dans les matériaux argileux : application aux bentonites compactées des  
844 barrières ouvragées. Université de Poitiers, Poitiers-France.

845 Pusch, R., 1979. Highly Compacted Sodium Bentonite for Isolating Rock-Deposited  
846 Radioactive Waste Products. *Journal Nuclear Technology* 45, 153–157.  
847 <https://doi.org/10.13182/NT79-A32305>  
848 Reinholdt, M.X., Hubert, F., Faurel, M., Tertre, E., Razafitianamaharavo, A., Francius, G.,  
849 Prêt, D., Petit, S., Béré, E., Pelletier, M., Ferrage, E., 2013. Morphological properties  
850 of vermiculite particles in size-selected fractions obtained by sonication. *Applied Clay*  
851 *Science* 77–78, 18–32. <https://doi.org/10.1016/j.clay.2013.03.013>  
852 Sakharov, B.A., Drits, V.A., McCarty, D.K., Walker, G.M., 2016. Modeling Powder X-Ray  
853 Diffraction Patterns of the Clay Minerals Society Kaolinite Standards: Kga-1, Kga-1b,  
854 and Kga-2. *Clays Clay Miner.* 64, 314–333.  
855 <https://doi.org/10.1346/CCMN.2016.0640307>  
856 Sato, H., 2000. The Effect of Pore Structural Factors on Diffusion in Compacted Sodium  
857 Bentonite. *MRS Proc.* 663, 605. <https://doi.org/10.1557/PROC-663-605>

858 Sato, H., Suzuki, S., 2003. Fundamental study on the effect of an orientation of clay particles  
859 on diffusion pathway in compacted bentonite. *Applied Clay Science* 23, 51–60.  
860 [https://doi.org/10.1016/S0169-1317\(03\)00086-3](https://doi.org/10.1016/S0169-1317(03)00086-3)

861 Savoye, S., Beaucaire, C., Grenut, B., Fayette, A., 2015. Impact of the solution ionic strength  
862 on strontium diffusion through the Callovo-Oxfordian clayrocks: An experimental and  
863 modeling study. *Applied Geochemistry* 61, 41–52.  
864 <https://doi.org/10.1016/j.apgeochem.2015.05.011>

865 Shackelford, C.D., Moore, S.M., 2013. Fickian diffusion of radionuclides for engineered  
866 containment barriers: Diffusion coefficients, porosities, and complicating issues.  
867 *Engineering Geology* 152, 133–147. <https://doi.org/10.1016/j.enggeo.2012.10.014>

868 Skipper, N.T., Lock, P.A., Titiloye, J.O., Swenson, J., Mirza, Z.A., Howells, W.S.,  
869 Fernandez-Alonso, F., 2006. The structure and dynamics of 2-dimensional fluids in  
870 swelling clays. *Chemical Geology* 230, 182–196.  
871 <https://doi.org/10.1016/j.chemgeo.2006.02.023>

872 Suzuki, S., Sato, H., Ishidera, T., Fujii, N., 2004. Study on anisotropy of effective diffusion  
873 coefficient and activation energy for deuterated water in compacted sodium bentonite.  
874 *Journal of Contaminant Hydrology* 68, 23–37. [https://doi.org/10.1016/S0169-7722\(03\)00139-6](https://doi.org/10.1016/S0169-7722(03)00139-6)

875 Swenson, J., Bergman, R., Howells, W.S., 2000. Quasielastic neutron scattering of two-  
876 dimensional water in a vermiculite clay. *J. Chem. Phys.* 113, 2873–2879.  
877 <https://doi.org/10.1063/1.1305870>

878

879 Tertre, E., Delville, A., Prêt, D., Hubert, F., Ferrage, E., 2015. Cation diffusion in the  
880 interlayer space of swelling clay minerals – A combined macroscopic and microscopic  
881 study. *Geochimica et Cosmochimica Acta* 149, 251–267.  
882 <https://doi.org/10.1016/j.gca.2014.10.011>

883 Tertre, E., Savoye, S., Hubert, F., Prêt, D., Dabat, T., Ferrage, E., 2018. Diffusion of Water  
884 through the Dual-Porosity Swelling Clay Mineral Vermiculite. *Environ. Sci. Technol.*  
885 52, 1899–1907. <https://doi.org/10.1021/acs.est.7b05343>

886 Titiloye, J.O., Skipper, N.T., 2001. Molecular dynamics simulation of methane in sodium  
887 montmorillonite clay hydrates at elevated pressures and temperatures. *Molecular*  
888 *Physics* 99, 899–906. <https://doi.org/10.1080/00268970010028863>

889 Tournassat, C., Steefel, C.I., 2019. Reactive Transport Modeling of Coupled Processes in  
890 Nanoporous Media. *Reviews in Mineralogy and Geochemistry* 85, 75–109.  
891 <https://doi.org/10.2138/rmg.2019.85.4>

892 Tyagi, M., Gimmi, T., Churakov, S.V., 2013. Multi-scale micro-structure generation strategy  
893 for up-scaling transport in clays. *Advances in Water Resources* 59, 181–195.  
894 <https://doi.org/10.1016/j.advwatres.2013.06.002>

895 Underwood, T.R., Bourg, I.C., 2020. Large-Scale Molecular Dynamics Simulation of the  
896 Dehydration of a Suspension of Smectite Clay Nanoparticles. *J. Phys. Chem. C* 124,  
897 3702–3714. <https://doi.org/10.1021/acs.jpcc.9b11197>

898 Valleau, J., Diestler, D., Cushman, J., Schoen, M., Hertzner, A., Riley, M., 1991. Comment  
899 on: Adsorption and diffusion at rough surfaces. A comparison of statistical mechanics,  
900 molecular dynamics, and kinetic theory. *The Journal of Chemical Physics* 95, 6194–  
901 6195.

902 Van Loon, L.R., Soler, J.M., Jakob, A., Bradbury, M.H., 2003. Effect of confining pressure  
903 on the diffusion of HTO,  $^{36}\text{Cl}^-$  and  $^{125}\text{I}^-$  in a layered argillaceous rock (Opalinus  
904 Clay): diffusion perpendicular to the fabric. *Applied Geochemistry* 18, 1653–1662.  
905 [https://doi.org/10.1016/S0883-2927\(03\)00047-7](https://doi.org/10.1016/S0883-2927(03)00047-7)

- 906 Van Loon, L.R., Soler, J.M., Müller, W., Bradbury, M.H., 2004. Anisotropic Diffusion in  
907 Layered Argillaceous Rocks: A Case Study with Opalinus Clay. *Environ. Sci.*  
908 *Technol.* 38, 5721–5728.
- 909 Wenk, H.-R., Kanitpanyacharoen, W., Voltolini, M., 2010. Preferred orientation of  
910 phyllosilicates: Comparison of fault gouge, shale and schist. *Journal of Structural*  
911 *Geology* 12, 478-489.
- 912 Wenk, Voltolini, Mazurek, Loon, V.L.R., Vinsot, 2008. Preferred Orientations and  
913 Anisotropy in Shales: Callovo-Oxfordian Shale (France) and Opalinus Clay  
914 (Switzerland). *Clays Clay Miner.* 56, 285–306.  
915 <https://doi.org/10.1346/CCMN.2008.0560301>
- 916 Wittebroodt, C., Savoye, S., Frasca, B., Gouze, P., 2012. Diffusion of HTO,  $^{36}\text{Cl}^-$  and  $^{125}\text{I}^-$  in  
917 Upper Toarcian argillite samples from Tournemire: Effects of initial iodide  
918 concentration and ionic strength. *Applied Geochemistry* 27, 1432-1441.
- 919 Xiang, Y., Al, T., Scott, L., Loomer, D., 2013. Diffusive anisotropy in low-permeability  
920 Ordovician sedimentary rocks from the Michigan Basin in southwest Ontario. *Journal*  
921 *of Contaminant Hydrology* 155, 31-45.
- 922

## 923 **6. Supplementary data (S. D.)**

### 924 **S.1. Materials and methods**

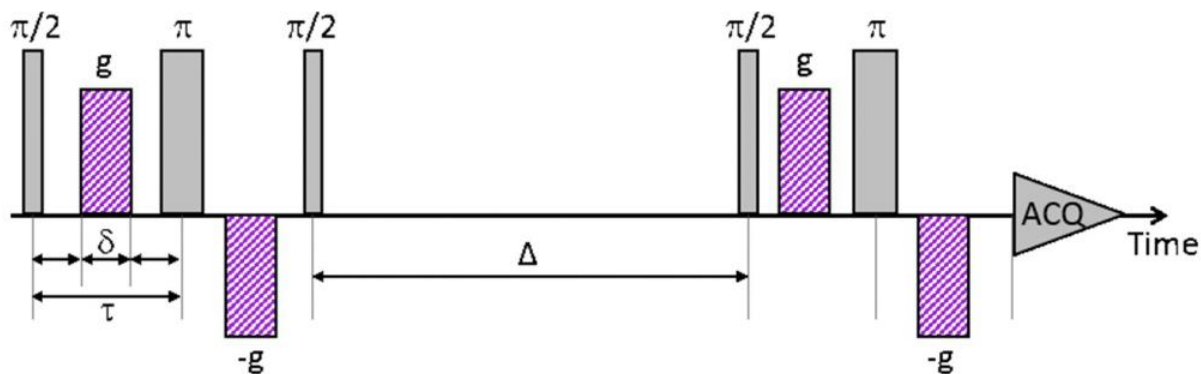
#### 925 *S.1.1. $^1\text{H}$ NMR Pulsed Gradient Spin Echo experiments*

926 The Pulsed Gradient Spin Echo attenuation measurements by Nuclear Magnetic  
927 Resonance (PGSE-NMR) analyses were performed at the ICMN laboratory (Orléans, France)  
928 on the Na-kaolinite compacted sample. The dried Na-kaolinite samples, in volume-constrained  
929 Polyether ether ketone (PEEK) tubes (see [Section S.1.1](#)), were first water-saturated by capillary  
930 imbibition. To do so, the bottom part of the sample was put in contact with deionized water,  
931 while the other side of the tube was connected to a primary vacuum pump to favor water  
932 migration and gentle evacuation of air from the pore network. The NMR measurements were  
933 performed using the same setup and experimental conditions as in ([Porion et al., 2018](#); [Dabat](#)  
934 [et al., 2020](#)) on a Bruker<sup>®</sup> DSX100 spectrometer. This instrument operates with a static  
935 magnetic field of 2.35 T and is equipped with a saddle detection coil and a micro-imaging probe  
936 (Micro5 Bruker) with gradient coils to generate magnetic field gradients in three perpendicular  
937 directions. The macroscopic water mobility along any pre-selected direction within the sample

938 was determined based on  $^1\text{H}$  PGSE-NMR attenuation measurements (Stejskal and Tanner,  
 939 1965; Cotts et al., 1989; Callaghan, 1991) by using the pulse sequence illustrated in Fig. S1.  
 940 The largest wave vector ( $q_{\text{MAX}}$ ) associated with these attenuation measurements is defined as  
 941  $q_{\text{MAX}} = \frac{\gamma \cdot \delta \cdot G_{\text{MAX}}}{\pi} = 6.81 \cdot 10^4 \text{ m}^{-1}$ , where  $\gamma$  is the proton gyromagnetic ratio ( $2.6752 \cdot 10^8 \text{ rad/s}$  for  
 942  $^1\text{H}$ ),  $\delta$  is the duration of each applied field gradient (i.e., 0.5 ms) (see Fig. S1) and  $G_{\text{MAX}}$  is the  
 943 largest applied field gradient (i.e., 1.6 Tesla  $\text{m}^{-1}$ ). Accordingly, the spatial length over which  
 944 the dynamics of the water is investigated is larger than 15  $\mu\text{m}$ . For these experiments, the  
 945 diffusion time ( $\Delta$ ) and the delay ( $\tau$ ) were set to 20 ms and 760  $\mu\text{s}$ , respectively (Fig. S1). The  
 946 attenuation of the intensity of the NMR echo  $I(q)/I(0)$  evolves according to a Gaussian  
 947 relationship from which the components of the self-diffusion tensor are easily extracted (Cotts  
 948 et al., 1989; Callaghan, 1991):

$$949 \quad \frac{I(q)}{I(0)} = \exp\left[-4 \pi^2 q^2 \vec{e}_g^T \overleftrightarrow{D_p} \vec{e}_g (\Delta + 3\tau/2 - \delta/6)\right] \quad (\text{S1})$$

950 where  $\vec{e}_g$  is the direction of the applied field gradient, and  $\overleftrightarrow{D_p}$  is the self-diffusion tensor. The  
 951 pulsed gradients were applied along six non-collinear directions (Basser et al., 1994; Skare et  
 952 al., 2000) noted  $\vec{e}_1 = \vec{e}_x = (1,0,0)$ ,  $\vec{e}_2 = \vec{e}_y = (0,1,0)$ ,  $\vec{e}_3 = \vec{e}_z = (0,0,1)$ ,  $\vec{e}_4 =$   
 953  $(1/\sqrt{2}, 1/\sqrt{2}, 0)$ ,  $\vec{e}_5 = (0, 1/\sqrt{2}, 1/\sqrt{2})$  and  $\vec{e}_6 = (1/\sqrt{2}, 0, 1/\sqrt{2})$ , respectively, with the  
 954 direction  $\vec{e}_3$  being parallel to the compaction/centrifugation axis of the clay sample. From the  
 955 six corresponding components of the water self-diffusion tensor, one can easily extract its three  
 956 principal axes and the corresponding eigenvalues that describe the water mobility in the  
 957 longitudinal or transverse direction of the tube axis. The PGSE-NMR attenuation measurements  
 958 were performed at  $\sim 19^\circ\text{C}$  (i.e., 292 K), and the associated experimental bulk water self-  
 959 diffusion coefficient  $D_0$  was measured at  $2.0 \pm 0.5 \cdot 10^{-9} \text{ m}^2 \text{ s}^{-1}$  in these conditions.



960

961 **Fig. S1.** Pulse sequence used to perform Pulsed Gradient Spin Echo (PGSE-NMR) attenuation  
 962 measurements in Na-kaolinite samples.

963

964 **. Induration of the samples and two-dimensional X-Ray Scattering measurements**

965 For each sample used in this study, a duplicate was prepared to be used for particle  
 966 organization measurements. Induration of the duplicate samples was performed to produce thin  
 967 sections for two-dimensional X-Ray Scattering (2D-XRS) measurements. The induration  
 968 method used here was based on the thermal impregnation technique with methyl methacrylate  
 969 (MMA, C<sub>5</sub>H<sub>8</sub>O<sub>2</sub>), which was developed by [Sammaljärvi et al. \(2012\)](#) and successfully applied  
 970 for Na-kaolinite samples ([Dabat et al., 2020](#)). The duplicates for 2D-XRS were prepared in  
 971 PEEK tubes (diameter of 0.64 cm and height of 7.5 cm) instead of PMMA because the latter  
 972 can dissolve when in contact with MMA. Perforated PEEK caps and cellulose membrane with  
 973 a pore size of 0.1 μm were placed at each side to maintain both the total porosity and particle  
 974 organization of the sample during the induration process. The duplicates were first placed under  
 975 a vacuum for 20 minutes to remove the residual water that could interfere with the  
 976 polymerization of MMA. Then, liquid MMA mixed with thermal initiator benzoyl peroxide  
 977 (BPO, at 5% of MMA mass) was introduced into the tubes without breaking the vacuum to  
 978 facilitate the access of MMA gas to the smallest pores. The samples were kept in contact with  
 979 liquid MMA for a few days up to two weeks (in the case of centrifuged Na-vermiculite) to  
 980 promote as much as possible the capillary saturation of the pores by the MMA+BPO mixture.

981 After saturation, the PEEK tubes that contained clayey samples were sealed with PTFE caps  
982 and placed in a water bath at 55°C for at least 24 hours to complete the polymerization of MMA  
983 into PMMA.

984 Following the induration process, the obtained samples were cut longitudinally and  
985 transversely with respect to the tube axis (Fig. 2a) using a circular saw (Fig. 2b). The resulting  
986 lamellas were reduced by a polishing table to 500 μm thickness to allow sufficient transmission  
987 for the XRS measurements (Dabat et al., 2020). Acquisition of two-dimensional XRS (2D-  
988 XRS) patterns for anisotropy in particle orientation measurements was performed at the  
989 Laboratoire de Physique des Solides (LPS) - Orsay, France. The X-ray beam is generated via a  
990 copper rotating anode generator (RU H3R, Rigaku Corporation, Japan), equipped with a  
991 multilayer W/Si mirror (Osmic), which generates a monochromatic beam ( $\lambda_{\text{CuK}\alpha} = 1.5418 \text{ \AA}$ )  
992 with a spot size of 1 mm<sup>2</sup> that passes through the slits to cover a 600 x 600 μm<sup>2</sup> surface of the  
993 sample. The scattering signals (Fig. 2c) from the sample were collected on a 2D-detector  
994 (MAR345, marXperts GmbH®, Germany, 150-μm pixel size). The sample-to-detector distance  
995 was set to 250 mm. This configuration makes it possible to reach a scattering vector modulus  
996 down to  $Q_{\text{min}} = 0.2 \text{ \AA}^{-1}$  ( $Q = 2\pi/d = 4\pi/\lambda \sin(\theta_B)$ , where  $\lambda$  is the incident wavelength, and  $2\theta_B$   
997 is the scattering angle). The sample lamellas were aligned perpendicular to the incident X-ray  
998 beam by mounting them on a goniometer head, and the XRS were acquired with a typical  
999 acquisition time of 900 s.

### 1000 *S.1.3. Through-diffusion experiments on the HDO tracer*

1001 The experimental setup for the Through-Diffusion (TD) experiments on the water tracer  
1002 (HDO) was previously used by Tertre et al. (2018) and originally adapted from the one proposed  
1003 by Van Loon et al. (2003). The configurations of this setup allow for measuring HDO diffusion  
1004 along the z-direction, i.e., perpendicular to the compaction plane and the preferred orientation  
1005 of the clay particles. It consists of a fluid circulation system and a PMMA tube that contains

1006 the clay sample compacted at the desired  $\varepsilon$  value (see [section 2.2](#) in the original text). The  
1007 sample is retained in the tube via a series of components on each side, listed from the closest to  
1008 the sample to the farthest, as follows: (i) cellulose membrane with a pore size of 0.1  $\mu\text{m}$ , (ii) a  
1009 stainless-steel filter (pore diameter of 10  $\mu\text{m}$ ), and (iii) two PEEK grids (nominal spaces of 280  
1010 and 450  $\mu\text{m}$  for mono filaments with diameters equal to 120 and 200  $\mu\text{m}$ , respectively). The  
1011 PEEK grids are used to homogenize the flow of the solution that arrives at each side of the  
1012 sample ([Melkior, 2000](#)). The fluid circulation system consists of two 50-mL reservoirs (i.e.,  
1013 upstream, and downstream reservoirs) and a peristaltic pump used to ensure the constant  
1014 circulation of the solutions. Prior to the TD experiment, the sample was saturated with Milli-  
1015 Q<sup>®</sup> water ( $\sim 18.2 \text{ M}\Omega \text{ cm}$ ) by maintaining circulation of the water on each side of it for two  
1016 weeks ([Tertre et al., 2018](#)).

1017 For the TD experiments, the upstream reservoir was filled with 50 mL of a 0.01-M NaCl  
1018 solution, spiked with HDO at 0.55 M and prepared by a dilution of initial D<sub>2</sub>O solution (purity  
1019 of 99.8 atom % D purchased from Agros Organics<sup>®</sup>), and the downstream reservoir was filled  
1020 with 50 mL of Milli-Q water. The 0.01-M NaCl solution was used in the upstream reservoir to  
1021 to measure the in addition to HDO the diffusion of ions (i.e., Na<sup>+</sup>, Cl<sup>-</sup>) as performed previously  
1022 in [Tertre et al. \(2018\)](#); data which are not reported in this present study. The two reservoirs were  
1023 then connected to the TD setup, and  $t=0$  was set as the fluid circulation started. To keep the  
1024 HDO concentration gradient as constant as possible between the two reservoirs, both reservoirs  
1025 were regularly replaced with fresh ones (the time step can vary between a few hours to 1 day  
1026 depending on the experiments), and 1 mL aliquot from the reservoirs were collected for the  
1027 HDO concentration measurements. The results from the upstream reservoirs (not shown)  
1028 confirmed that the decrease in the HDO concentration did not exceed 3%, which validated the  
1029 hypothesis of a constant gradient of HDO during the experiment (see below for the boundary  
1030 conditions).

1031 All of the TD experiments were performed in a climate-controlled room under a  
 1032 temperature of  $20 \pm 1$  °C. The HDO concentrations were determined by water isotope analysis  
 1033 (LWIA DLT-100, Los Gatos Research), and the amount of HDO diffusing in the downstream  
 1034 reservoir was calculated by accounting for the HDO concentration that was naturally present in  
 1035 ultrapure water (i.e.,  $1.6529 \times 10^{-2}$  M), as performed in [Tertre et al. \(2018\)](#).

1036 The results from the TD experiments were analyzed by resolving the classical Fick's  
 1037 second law for one-dimensional transport:

$$1038 \quad \frac{\partial C}{\partial t} = \frac{D_e}{\alpha} \cdot \frac{\partial^2 C}{\partial x^2} = \frac{D_e}{\varepsilon + \rho_{\text{app}} K_d} \frac{\delta^2 C}{\partial x^2} \quad (\text{S2})$$

1039 where  $C$  is the aqueous concentration ( $\text{mol m}^{-3}$ ),  $t$  is the time (s),  $D_e$  is the effective diffusion  
 1040 coefficient ( $\text{m}^2 \text{s}^{-1}$ ),  $K_d$  is the distribution coefficient ( $\text{m}^3 \text{kg}^{-1}$ ),  $\rho_{\text{app}}$  is the bulk dry density ( $\text{kg}$   
 1041  $\text{m}^{-3}$ ), and  $\alpha$  is the rock capacity factor. For the water tracer (-), if no adsorption occurs, then  $\alpha$   
 1042 is equal to  $\varepsilon$ , while if adsorption occurs,  $\alpha$  could be greater than  $\varepsilon$ . Eq. (S2) was resolved by  
 1043 using the following initial and boundary conditions:

$$1044 \quad C(x, t) = 0 \text{ for } t = 0 \quad (\text{S3})$$

$$1045 \quad C(x, t) = C_o \text{ at } x = 0 \text{ for } t > 0 \quad (\text{S4})$$

$$1046 \quad C(x, t) = 0 \text{ at } x = L \text{ for } t > 0 \quad (\text{S5})$$

1047 where  $C_o$  is the HDO concentration in the upstream reservoir ( $\text{mol m}^{-3}$ ) corrected from the  
 1048 natural concentration of HDO present in ultra-pure water, and  $L$  is the thickness of the sample  
 1049 (m). By considering these equations, the diffusive flux (i.e.,  $J(x=L, t)$  in  $\text{mol s}^{-1}$ ) in the  
 1050 downstream reservoir can be described according to Eq. (S6), as reported by [Crank \(1975\)](#):

$$1051 \quad J(x = L, t) = \frac{S C_o D_e}{L} \left( 1 + 2 \sum_{n=1}^{\infty} (-1)^n \exp\left(\frac{-D_e n^2 \pi^2 t}{\alpha L^2}\right) \right) \quad (\text{S6})$$

1052 where  $S$  is the cross-sectional area perpendicular to the diffusive direction ( $\text{m}^2$ ). The  
 1053 corresponding total amount of cumulative tracer in the downstream reservoir (i.e.,  $n(x=L, t)$  in  
 1054 mol) is as follows:

1055 
$$n(x = L, t) = SC_0 L \left( \frac{D_e}{L^2} t - \frac{\alpha}{6} - \frac{2\alpha}{\pi^2} \sum_{n=1}^{\infty} \frac{(-1)^n}{n^2} \exp \left( -\frac{D_e n^2 \pi^2}{L^2} t \right) \right) \quad (\text{S7})$$

1056 As done in [Tertre et al. \(2018\)](#), the diffusion parameters (i.e.,  $D_e$  and  $\alpha$ ) were obtained  
1057 by least-square fitting of the experimental results of the diffusive flux incoming in the  
1058 downstream reservoir. To accomplish that step, fully analytical solutions were obtained in  
1059 Laplace space and were then subsequently numerically inverted to provide the solution in time  
1060 (more details in [Savoie et al., 2015](#)). Fitting procedures were performed by accounting for  
1061 diffusion in stainless-steel filters, as performed in [Tertre et al. \(2018\)](#). Uncertainties in both  $D_e$   
1062 and  $\alpha$  were calculated by considering the uncertainties in the measured tracer fluxes  
1063 (corresponding to the uncertainty in the concentration measurements; see [Table 1](#)).

#### 1064 ***S.1.4. Generation of virtual porous media for Brownian dynamics simulation***

1065 Mesoscale Brownian dynamics simulations of water diffusion in both Na-vermiculite and  
1066 Na-kaolinite as a function of the anisotropy in the particles' orientation were performed on 3D  
1067 virtual porous media (VPM; see [Table S1](#)), mimicking the distribution of the shapes and sizes  
1068 of the particles in these samples. The description of the generation of these VPM has been  
1069 extensively described elsewhere ([Ferrage et al., 2015](#); [Dabat et al., 2018, 2020](#)). Briefly, the  
1070 particles are allowed to settle in a square simulation box with periodic conditions along the  $x$   
1071 and  $y$  axes ( $z$  axis pointing upward; [Fig. 2a](#)), according to a steepest descent algorithm to reduce  
1072 the barycenter altitude. A log normal distribution in the dimensions (i.e., basal surface, particle  
1073 diameter, ratio between thickness and diameter, and ellipticity degree) of the individual  
1074 particles was obtained from the work of [Ferrage et al. \(2015\)](#) and based on the experimental  
1075 morphological study of [Reinholdt et al. \(2013\)](#) for the 0.1–0.2  $\mu\text{m}$  size fraction of vermiculite  
1076 from Santa Olalla, Spain, investigated here. During the settling process, the particles are  
1077 allowed to slide, swivel or rotate with a random amplitude that ranges from zero to a maximum  
1078 value. A wide range of degree of anisotropy in the particles' orientation is then obtained by  
1079 tuning the amplitudes of the movements, leading to a variation in the degree of freedom in the

1080 particle motions (Ferrage et al., 2015). This degree of anisotropy of the particles' orientation  
1081 was extracted by calculating the average of the second-order Legendre polynomial on the  
1082 angular distribution of the particle orientations, as follows:

$$1083 \quad \langle P_2 \rangle = \langle P_2(\cos\theta) \rangle = \langle 3\cos^2\theta - 1 \rangle / 2 \quad (\text{S8})$$

1084 where  $\theta$  is the angle between the normal unit vector of the particle and the  $z$  axis of the  
1085 simulation box (Fig. 4a). This  $\langle P_2 \rangle$  order parameter, also referred to as the nematic order  $S$   
1086 (Dabat et al., 2018; Underwood and Bourg, 2020) or the Hermans parameter  $H$  (Hermans and  
1087 Platzek, 1939), takes the value of 0 for an isotropic organization and 1 when all of the particles  
1088 are perfectly oriented in the bedding (all normal to the particles aligned with the  $z$  axis of the  
1089 simulation box).

1090 To cover over a large range of anisotropy degrees in particle orientations, 13 particle  
1091 packings with  $\langle P_2 \rangle$  values that varied from 0.03 to 0.96 were generated according to this  
1092 algorithm ((Ferrage et al., 2018; Dabat et al., 2020); see Table S1 and Fig. 4a). This  
1093 methodology leads, however, to different interparticle porosity values as a function of  $\langle P_2 \rangle$  and  
1094 does not allow obtaining periodic conditions in the  $z$  direction. To overcome these drawbacks  
1095 for the BD simulations, additional treatments, as detailed by Dabat et al. (2020), were applied  
1096 to the different obtained VPM. Briefly, a cubic sub-volume of  $\sim 2000$  particles was first  
1097 extracted, and particles were then polygonized considering 12 in-plane vectors plus 2 vectors  
1098 passing along the normal of the particles. Periodic conditions with the minimum-image  
1099 convention were applied along the three directors,  $\vec{e}_x$ ,  $\vec{e}_y$ , and  $\vec{e}_z$ , of the simulation box. Based  
1100 on the obtained sub-volumes, two subsequent treatments were applied to reduce the interparticle  
1101 porosity of the packings and to reach an interparticle porosity value that is close to that of the  
1102 water-saturated samples analyzed in this study by PGSE-NMR and through-diffusion  
1103 experiments, i.e.,  $\epsilon_{\text{interp.}} \sim 0.25$  (Dabat et al., 2020). The first treatment consists of allowing each  
1104 particle to grow along its 14 vectors, with detection and rejection of particle overlapping. The

1105 second treatment implies the injection of a new particle on the surface of an existing particle  
1106 and the subsequent particle growth to fill the porosity. The two processes led to final  
1107 interparticle porosity values of approximately 0.27 for packings with  $0.03 \leq \langle P_2 \rangle \leq 0.85$  and  
1108 approximately 0.25 for packings with  $\langle P_2 \rangle = 0.92$  and  $0.96$  (Table S1; Fig. 4a). Because these  
1109 treatments lead to a decrease in the particle sizes and thus an increase in the overall specific  
1110 surface areas (SSA) of the sample, a last treatment involved the dilatation of the simulation box  
1111 (and thus particle) dimensions. For vermiculite, the final cubic lengths of the VPM are  $\sim 1 \mu\text{m}$   
1112 (i.e., between 1.12 and 0.99 for the order parameter  $\langle P_2 \rangle$  ranging from 0.03 to 0.96, respectively;  
1113 see Table S1) and of the SSA values are  $\sim 95 \text{ m}^2 \text{ g}^{-1}$ , which is in agreement with the experimental  
1114 results from Reinholdt et al. (2013). The total number of particles ranges between  $\sim 11000$  and  
1115  $\sim 7400$ , for the more isotropic and anisotropic organizations, respectively (Table S1).

1116

1117

1118

1119

1120

1121

1122

1123

1124

1125 **Table S. 1.**

1126 Characteristics of the 13 virtual porous media used for the Brownian dynamics simulations.  
 1127 The  $\langle P_2 \rangle$  and  $\varepsilon_{\text{interp.}}$  values stand for the order parameter and the interparticle porosity,  
 1128 respectively. The  $N_{\text{part.}}$  and  $\ell_{\text{box}}$  parameters stand for the total number of particles and the cubic  
 1129 length of the simulation box (in  $\mu\text{m}$ ), respectively.

| Pack. # | $\langle P_2 \rangle$ | $\varepsilon_{\text{interp.}}$ | $N_{\text{part.}}$ | $\ell_{\text{box}}$ |
|---------|-----------------------|--------------------------------|--------------------|---------------------|
| 1       | 0.028                 | 0.272                          | 10639              | 1.12                |
| 2       | 0.053                 | 0.274                          | 10932              | 1.12                |
| 3       | 0.104                 | 0.271                          | 11039              | 1.13                |
| 4       | 0.208                 | 0.272                          | 11139              | 1.13                |
| 5       | 0.322                 | 0.272                          | 11307              | 1.12                |
| 6       | 0.392                 | 0.275                          | 11092              | 1.12                |
| 7       | 0.489                 | 0.273                          | 11139              | 1.15                |
| 8       | 0.575                 | 0.275                          | 11404              | 1.15                |
| 9       | 0.718                 | 0.269                          | 11446              | 1.16                |
| 10      | 0.800                 | 0.264                          | 11693              | 1.16                |
| 11      | 0.849                 | 0.264                          | 11863              | 1.18                |
| 12      | 0.915                 | 0.249                          | 11526              | 1.18                |
| 13      | 0.963                 | 0.253                          | 7403               | 0.99                |

1130

1131 **References for supplementary data**

1132  
 1133 Basser, P.J., Mattiello, J., Lebihan, D., 1994. Estimation of the Effective Self-Diffusion  
 1134 Tensor from the NMR Spin Echo. *Journal of Magnetic Resonance, Series B* 103, 247–  
 1135 254. <https://doi.org/10.1006/jmrb.1994.1037>  
 1136 Callaghan, P.T., 1991. Principles of nuclear magnetic resonance microscopy. Clarendon  
 1137 Press.  
 1138 Cotts, R.M., Hoch, M.J.R., Sun, T., Markert, J.T., 1989. Pulsed field gradient stimulated echo  
 1139 methods for improved NMR diffusion measurements in heterogeneous systems.  
 1140 *Journal of Magnetic Resonance* (1989) 83, 252–266. [https://doi.org/10.1016/0022-](https://doi.org/10.1016/0022-2364(89)90189-3)  
 1141 [2364\(89\)90189-3](https://doi.org/10.1016/0022-2364(89)90189-3)  
 1142 Crank, J., 1975. *The Mathematics of Diffusion*, 2nd ed. Oxford University Press: London.  
 1143 Dabat, T., Porion, P., Hubert, F., Paineau, E., Dzas, B., Grégoire, B., Tertre, E., Delville, A.,  
 1144 Ferrage, E., 2020. Influence of preferred orientation of clay particles on the diffusion of

1145 water in kaolinite porous media at constant porosity. *Applied Clay Science* 184, 105354.  
1146 <https://doi.org/10.1016/j.clay.2019.105354>

1147 Dabat, T., Mazurier, A., Hubert, F., Tertre, E., Grégoire, B., Dazas, B., Ferrage, E., 2018.  
1148 Mesoscale Anisotropy in Porous Media Made of Clay Minerals. A Numerical Study  
1149 Constrained by Experimental Data. *Materials* 11, 1972.  
1150 <https://doi.org/10.3390/ma11101972>

1151 Ferrage, E., Hubert, F., Tertre, E., Delville, A., Michot, L.J., Levitz, P., 2015. Modeling the  
1152 arrangement of particles in natural swelling-clay porous media using three-  
1153 dimensional packing of elliptic disks. *Physical Review E* 91, 062210.  
1154 <https://doi.org/10.1103/PhysRevE.91.062210>

1155 Ferrage, E., Hubert, F., Baronnet, A., Grauby, O., Tertre, E., Delville, A., Bihannic, I., Prêt,  
1156 D., Michot, L.J., Levitz, P., 2018. Influence of crystal structure defects on the small-  
1157 angle neutron scattering/diffraction patterns of clay-rich porous media. *J Appl*  
1158 *Crystallogr* 51, 1311–1322. <https://doi.org/10.1107/S160057671801052X>

1159 Melkior, T., 2000. Etude méthodologique de la diffusion de cations interagissant dans des  
1160 argiles : application : mise en œuvre expérimentale et modélisation du couplage  
1161 chimie-diffusion d'alcalins dans une bentonite synthétique (Ph.D. Thesis). Ecole  
1162 Centrale Paris, Paris, France.

1163 Hermans, P.H., Platzek, P., 1939. Beiträge zur Kenntnis des Deformationsmechanismus und  
1164 der Feinstruktur der Hydratzellulose. *Kolloid-Z, Kolloid-Z* 88, 68–72.

1165 Porion, P., Ferrage, E., Hubert, F., Tertre, E., Dabat, T., Faugère, A.M., Condé, F., Warmont,  
1166 F., Delville, A., 2018. Water Mobility within Compacted Clay Samples: Multi-Scale  
1167 Analysis Exploiting <sup>1</sup>H NMR Pulsed Gradient Spin Echo and Magnetic Resonance  
1168 Imaging of Water Density Profiles. *ACS Omega* 3, 7399–7406.  
1169 <https://doi.org/10.1021/acsomega.8b01083>

1170 Reinholdt, M.X., Hubert, F., Faurel, M., Tertre, E., Razafitianamaharavo, A., Francius, G.,  
1171 Prêt, D., Petit, S., Béré, E., Pelletier, M., Ferrage, E., 2013. Morphological properties  
1172 of vermiculite particles in size-selected fractions obtained by sonication. *Applied Clay*  
1173 *Science* 77–78, 18–32. <https://doi.org/10.1016/j.clay.2013.03.013>

1174 Sammaljärvi, J., Jokelainen, L., Ikonen, J., Siitari-Kauppi, M., 2012. Free radical  
1175 polymerisation of MMA with thermal initiator in brick and Grimsel granodiorite.  
1176 *Engineering Geology* 135–136, 52–59. <https://doi.org/10.1016/j.enggeo.2012.03.005>

1177 Savoye, S., Beaucaire, C., Grenut, B., Fayette, A., 2015. Impact of the solution ionic strength  
1178 on strontium diffusion through the Callovo-Oxfordian clayrocks: An experimental and  
1179 modeling study. *Applied Geochemistry* 61, 41–52.  
1180 <https://doi.org/10.1016/j.apgeochem.2015.05.011>

1181 Skare, S., Hedehus, M., Moseley, M.E., Li, T.-Q., 2000. Condition Number as a Measure of  
1182 Noise Performance of Diffusion Tensor Data Acquisition Schemes with MRI. *Journal*  
1183 *of Magnetic Resonance* 147, 340–352. <https://doi.org/10.1006/jmre.2000.2209>

1184 Stejskal, E.O., Tanner, J.E., 1965. Spin Diffusion Measurements: Spin Echoes in the Presence  
1185 of a Time-Dependent Field Gradient. *The Journal of Chemical Physics* 42, 288–292.  
1186 <https://doi.org/10.1063/1.1695690>